Nano Today 28 (2019) 100774

Contents lists available at ScienceDirect

Nano Today

journal homepage: www.elsevier.com/locate/nanotoday

Review

Noble metal-based 1D and 2D electrocatalytic nanomaterials: Recent progress, challenges and perspectives

Yiju Li [a,b,c], Shaojun Guo [a,b,c,*]

[a] Department of Materials Science and Engineering, College of Engineering, Peking University, Beijing 100871, PR China
[b] BIC-ESAT, College of Engineering, Peking University, Beijing 100871, PR China
[c] Beijing Key Laboratory for Magnetoeletric Materials and Devices (BKL-MEMD)

ARTICLE INFO

Article history:
Received 5 May 2019
Received in revised form 21 August 2019
Accepted 26 August 2019
Available online 21 September 2019

Keywords:
Renewable energy
Noble metals
One-dimensional
Two-dimensional
Electrocatalysis

ABSTRACT

Recently, one- (1D) and two-dimensional (2D) noble metal-based nanocrystals have triggered tremendous interest due to their unique anisotropic structure in the field of electrochemical energy conversion. In this review, we summarize the latest research developments in 1D and 2D noble metal-based nanocrystals with various nanostructures, and their potential applications as electrocatalysts toward fuel-cell-related electrocatalysis. Five strategies including size, shape, composition, surface, and interface engineering are proposed to rationally design the nanoarchitectures of the 1D and 2D noble metal-based electrocatalysts. In addition, we also highlight the underlying mechanisms behind the structure-property relationship. Finally, we conclude the current challenges and give our perspectives on the development of high-performance 1D and 2D noble metal-based electrocatalysts. We hope this review could offer timely information on the research of 1D and 2D noble metal-based nanocrystals and provide guidance for regulating their electrocatalytic properties.

Contents

Introduction

With the increasingly serious environmental problems and energy crisis, much effort has been devoted to the development of electrochemical energy conversion technologies that are clean, efficient and reliable. One of the biggest challenges in the utilization of high-efficiency electrochemical energy conversion technologies, such as fuel cell, metal-air battery, and water electrolysis, is to search the applicable electrocatalysts that are able to greatly lower the corresponding energy barrier for the electrochemical reactions, and simultaneously facilitate the electron charge transfer on the surface of electrode [1–3]. Over the past decade, a large variety of carbon and non-noble metal

* Corresponding author at: Department of Materials Science and Engineering, College of Engineering, Peking University, Beijing 100871, PR China.
E-mail address: guosj@pku.edu.cn (S. Guo).

https://doi.org/10.1016/j.nantod.2019.100774
1748-0132/

based electrocatalysts have been developed and achieved some success. Among these electrocatalysts, the heteroatom-doped carbon [4–11] and transition metal (Fe, Co, Ni, Mo, W) hydroxides/oxides/chalcogenides/carbides/phosphides/nitrides are the two most widely investigated categories [12–20]. It should be noted that, although the above-mentioned materials exhibit favorable electrocatalytic activities to specific reactions, their overall electrochemical performance is still far away from the corresponding noble metal-based electrocatalysts at present. The noble metal-based electrocatalysts remain the top priority in relevant industrial applications in despite of the scarcity and high cost. For example, Pt is the only efficient electrocatalyst in the proton exchange membrane fuel cells (PEMFCs), which is hardly to be replaced.

Noble metal-based nanoparticles loaded on carbon substrate are commercially available and extensively used as benchmarks in fuel-cell-related electrocatalytic applications, such as water electrolysis, oxygen electroreduction, and organic molecules electrooxidation. However, due to the insufficient reactivity, the carbon supported noble metal-based nanoparticles are still hard to be commercialized in these electrocatalytic technologies. In addition, the unsatisfactory stability of the carbon supported noble metal-based nanoparticles is another problem that further hinders their large-scale practical applications [21]. Owing to the point-to-point connection, the corrosion of carbon support and aggregation and dissolution of the commercial noble metal-based particulates can easily result in the activity loss, which is one of the major reasons for the rapid performance decay [22–25]. Faced with these challenging issues, the exploitation of new synthetic approaches for constructing noble metal-based nanocatalysts with optimized activity and durability, and minimum cost has become a hot and significant research topic. Among the noble metal-based electrocatalysts with various nanostructures, the 1D and 2D noble metal-based nanocatalysts with unique anisotropic structure have gained a great deal of research interest [26–34]. The structure asymmetry of the 1D and 2D nanocatalysts possesses higher resistibility to dissolution, aggregation and Ostwald ripening compared with the nanoparticle counterparts [35–38]. Moreover, the 1D and 2D nanocatalysts are less dependent on carbon supports and possess faster electron and mass transport [39–43]. Especially, the high surface-to-volume ratio in the 1D and 2D noble metal-based nanostructures endow them with numerous catalytically active sites exposed on the surface.

Besides the inherent architecture advantages of the 1D and 2D nanocatalysts, tremendous efforts have been devoted to further manipulating and regulating their chemical composition and physical structure to boost the electrocatalytic performance. Electrocatalysis occurs with the reactant molecules interaction with the catalytic surface of nanocatalysts. Factors that affect the electrocatalytic performance vary with different noble metal-based nanocrystals. Generally, size, shape, composition, surface and interface are five typical factors for tailoring the electrocatalytic performance of the 1D and 2D nanocatalysts. At the nanometer scale, the specific surface area and ratio of surface atoms to bulk atoms dramatically increase with the decrease of size of catalysts, so that the atom utilization can be greatly enhanced. Especially, when the diameter/thickness of the 1D/2D noble metal-based nanocatalysts are downsized to atomic scale, the surface low-coordination atoms are exposed to the largest extent, and the strain and electronic effects become prominent in some specific nanostructures, such as core-shell and heterogeneous nanostructures [44–46]. The shape of nanocatalysts determines the number of exposed active sites. Through adjusting the aspect ratio, various 1D (nanowires; nanotubes; nanorods; nanoribbons; nanochains; nanolances) [47–53] and 2D (nanoplates; nanosheets; nanodisks; nanorings) nanocatalysts [54–57] with abundant surface sites have been successfully synthesized. In addition, rationally manipulating the substructures of 1D and 2D nanocrystals, such as wavy nanowires and porous nanosheets, is another effective shape engineering strategy to enhance the electrocatalytic performance [58–64]. Composition including constituent elements and ratios is directly related with the intrinsic electrocatalytic performance. For the bimetallic and multimetallic nanocatalysts, the introduction of foreign metals can generate the synergetic (bifunctional) and ligand (electronic) effects, which are responsible for the enhanced electrocatalytic performance including activity and stability [65–69]. Ligand effect can cause a shift of the d-band center of metal atoms at the surface of electrocatalysts, resulting in optimized bonding of reactants and intermediates [70–73]. The improved electrochemical performance through the synergetic mechanism is to offer appropriate atom ensembles on the catalyst surface to accelerate the intermediate reactions [74–76]. It should be noted that, usually, it is hard to exactly distinguish the respective contribution in a bimetallic/multimetallic system. In most cases, synergistic and ligand effects would simultaneously contribute to an electrocatalytic process. Regulating the surface structures of the 1D and 2D nanocatalysts has become a popular research topic recently. The activity and selectivity of solid electrocatalysts are heavily dependent on the catalysts' surface structures. Tailoring surface structures of noble metal-based nanocrystals to expose different facets can exhibit different catalytic properties. For example, it is generally accepted that the specific activity in the oxygen reduction reaction (ORR) increases in the order of Pt(100) « Pt(111) ≈ Pt(110) in 0.1 M $HClO_4$ solution due to the electronic effect [77]. Furthermore, adjusting the numbers of specific atoms on the surface of catalysts is another effective surface engineering strategy to obtain high electrochemical performance. The most popular are the Pt and Pt-alloy skin and skeleton catalysts for ORR [78–80]. It is a promising approach to boost the intrinsic electrocatalytic activity while reducing the usage amount of Pt. Last but not the least, interface engineering has also been proved to be an effective method to optimize the electrochemical performance of nanocatalysts [81–84]. Apart from surface sites, interfacial sites between the primary and concomitant components are commonly where electrocatalytic reactions occur. In general, there are three types of interface interactions for the noble metal-based catalysts including metal/organic, metal/metal and metal/metal compound interfaces [85–88]. Primary noble metals and specific concomitant components need be rationally selected to manipulate the steric and electronic effects for optimizing the catalytic activity. Based on above discussions, it has been indicated that the performance of 1D and 2D noble metal-based electrocatalysts can be enhanced through reasonably regulating one or more structure parameters (size, shape, composition, surface and interface).

Great progress has been gained over the past few years in the synthesis of 1D and 2D noble metal-based electrocatalysts, but most of them have not been systematically summarized from the perspective of architecture design. To fill this gap, in this review, we place an emphasis on the rational design of 1D and 2D noble metal-based electrocatalysts with diverse nanostructures for boosting the fuel-cell-related electrochemical energy conversion reactions, such as ORR, methanol oxidation reaction (MOR), ethanol oxidation reaction (EOR), formic acid oxidation reaction (FAOR), hydrogen evolution reaction (HER) and oxygen evolution reaction (OER). Five typical engineering strategies, utilized to construct appropriate 1D and 2D architectures, were demonstrated in this review (Fig. 1). The structure-dependent mechanisms behind the optimized performance were detailly revealed and are expected to provide a guidance for the performance-oriented design of 1D and 2D electrocatalysts. Finally, we discussed the remaining challenges and came up with some perspectives on the development of more efficient

Fig. 1. Schematic illustration of various engineering strategies for the preparation of 1D and 2D noble metals as well as their electrocatalytic applications in ORR, EOR, FAOR, OER, HER and MOR.

fuel-cell-related 1D and 2D electrocatalysts featuring low cost and high activity and stability.

1D noble metal-based nanocrystals for electrocatalysis

1D noble metal and alloy based electrocatalysts

Compared with the zero-dimensional (0D) nanoparticles, highly anisotropic structure of the 1D nanocrystals leads to the enhanced electron and mass transport, preferential exposure of highly active facets and high resistibility to dissolution. Some works have indicated that 1D elemental Pt, Au, Ru, Ir, Rh and Pd nanocrystals show enhanced electrocatalytic activity and durability compared to the nanoparticle counterparts [89–94]. For example, the Pt nanowires (NWs) with a diameter of 47 ± 9.8 nm were prepared using a polymer template of track-etched polycarbonate (PCTE) membrane (Fig. 2a) [95]. The obtained Pt NWs catalyst shows a higher forward peak current density of 57.2 mA mg_{Pt}^{-1} than that of the commercial Pt/C (39.4 mA mg_{Pt}^{-1}) toward MOR. The improved performance is attributed to the enhancement of electron transfer and efficient utilization of Pt NWs while numerous Pt nanoparticle catalysts are prone to be embedded in the ionomer. Au also displays intriguing electrocatalytic activity for MOR. The ultralong and surfactant-free Au NWs were synthesized using the tellurium (Te) NWs as the sacrificial templates in aqueous solution [96]. The Au NWs with an average diameter of 22 ± 3 nm are interconnected with each other to form a uniform network (Fig. 2b and c). The crystal lattices in the high-resolution transmission electron microscope (HRTEM) image are measured to be 0.23 and 0.19 nm, which are attributed to the {111} and {200} lattice planes of fcc Au, respectively (inset in Fig. 2c). Owing to the absence of organic surfactant capping agents and intertwined network, the Au NWs stabilized by Br- ions exhibits higher activity than the Au NWs stabilized by CTAB and Au NPs (Fig. 2d).

Although the 1D unitary noble metal-based electrocatalysts display improved activity compared to the nanoparticulate counterparts, their performance can be further boosted by the incorporation of foreign atoms into the original matrix. The enhanced activity is usually attributed to the bifunctional and electronic effects in the bimetallic alloy systems. Recently, great progress has been gained in the controlled synthesis of 1D Pt-based bimetallic alloy catalysts with a broad composition range including PtCo, PtNi, PtFe, PtCu, PtAu, PtAg, and PtPd [97–103]. For instance, the three-dimensional (3D) Pt_3Co nanowire assemblies with adjustable compositions were synthesized through a facile solvothermal method [104]. As shown in Fig. 2e and f, the smooth Pt_3Co NWs with a diameter of 5–10 nm originate from the same center and stick out in various directions. It can be also found that each Pt_3Co nanowire branch is constructed with a stem and a cubic head. In addition, HRTEM image reveals that the lattice distance is about 0.22 nm, which is slightly smaller than that of the pure Pt (111) crystal plane (0.23 nm) (inset in Fig. 2f). The result suggests the successful incorporation of Co atoms into the Pt NWs. Fig. 2g shows the cyclic voltammetry (CV) curves of various samples toward MOR. The peak current density of the Pt_3Co nanowire assemblies (94 mA cm^{-2}) is much higher than that of Pt nanowire assemblies (61 mA cm^{-2}), and the peak oxidation potential is decreased by 50 mV. Since the Pt_3Co and Pt electrocatalysts have similar nanostructure, the improved performance should be derived from the introduction of Co atoms. The electronic effect induced by Co atoms could lower the binding energy of oxygenous intermediates on Pt and facilitate the cleavage of C–H bond. Furthermore, the Pt_3Co nanowire assemblies also display the enhanced stability compared with the commercial PtRu/CB and Pt/CB catalysts (Fig. 2h). The inferior stability of PtRu/CB and Pt/CB catalysts is mainly resulted from the serious corrosion of carbon substrate, which leads to the agglomeration and detachment of nanoparticles, while the Pt_3Co nanowire assemblies less suffer from this issue due to the unique 1D nanostructure. In most case, the dissolution of the base metal usually results in decreased activity and durability due to the surface atomic rearrangement. The formation of ordered intermetallic alloys is regarded as one of the most effective strategies to minimize the leaching of base metal and enhance the stability [105–108]. For example, the ordered intermetallic PtPb nanorods (NRs) were synthesized through a colloidal chemistry method, which exhibit much enhanced activity and stability for MOR compared with the commercial PtRu/C catalyst [109].

Compared with mono- and bi-metallic nanocrystals, multimetallic nanocrystals containing three or more metal elements may possess even better electrocatalytic properties owing to the more tunable components [110–112]. Recently, Yu's group reported a facile approach for the large-scale production of ultralong PtPdTe NWs using Te NWs as both sacrificial templates and reducing agents [113]. The optimal PtPdTe NWs show an enhanced activity toward MOR compared with the commercial Pt/C catalysts. The origin of the improved catalytic performance is illustrated in Fig. 2l. On one hand, the electronic structure of Pt modified by the adjacent Pd atoms could weaken the carbon monoxide (CO) adsorption and facilitate cleavage of C–H bond due to the shift of d-band center of Pt. On the other hand, the methanol molecules are decomposed on Pt sites to form Pt−CO, while Pd preferably catalyzes water molecules to form Pd−OH, which is used for accelerating CO oxidation to generate CO_2 and recover the active Pt sites. Hence, for the PtPdTe NWs with a low content of Pd ($Pt_{28}Pd_{15}Te_{57}$), there lack enough Pd sites for water dissociation to generate Pd−OH that accelerates the CO oxidation. For the PtPdTe NWs with a high content of Pd ($Pt_{16}Pd_{31}Te_{53}$), less Pt sites are available for methanol dehydrogenation, which could suppress the overall reaction kinetics. It follows that the optimal element content in the nanocatalysts could balance these effects to gain an optimized electrocatalytic performance. Inspired by the component effect in trimetallic nanocrystals toward MOR, the quaternary PtPdRuTe nanotubes (NTs) were further synthesized *via* a galvanic replacement reaction (Fig. 2 m–q) [114]. The Te atoms serve as the skeleton and minimize the usage amount of the other three noble metals. The Pt atoms are the active sites for the methanol dehydrogenation, while the oxyphilic Ru atoms contribute to the adsorption of

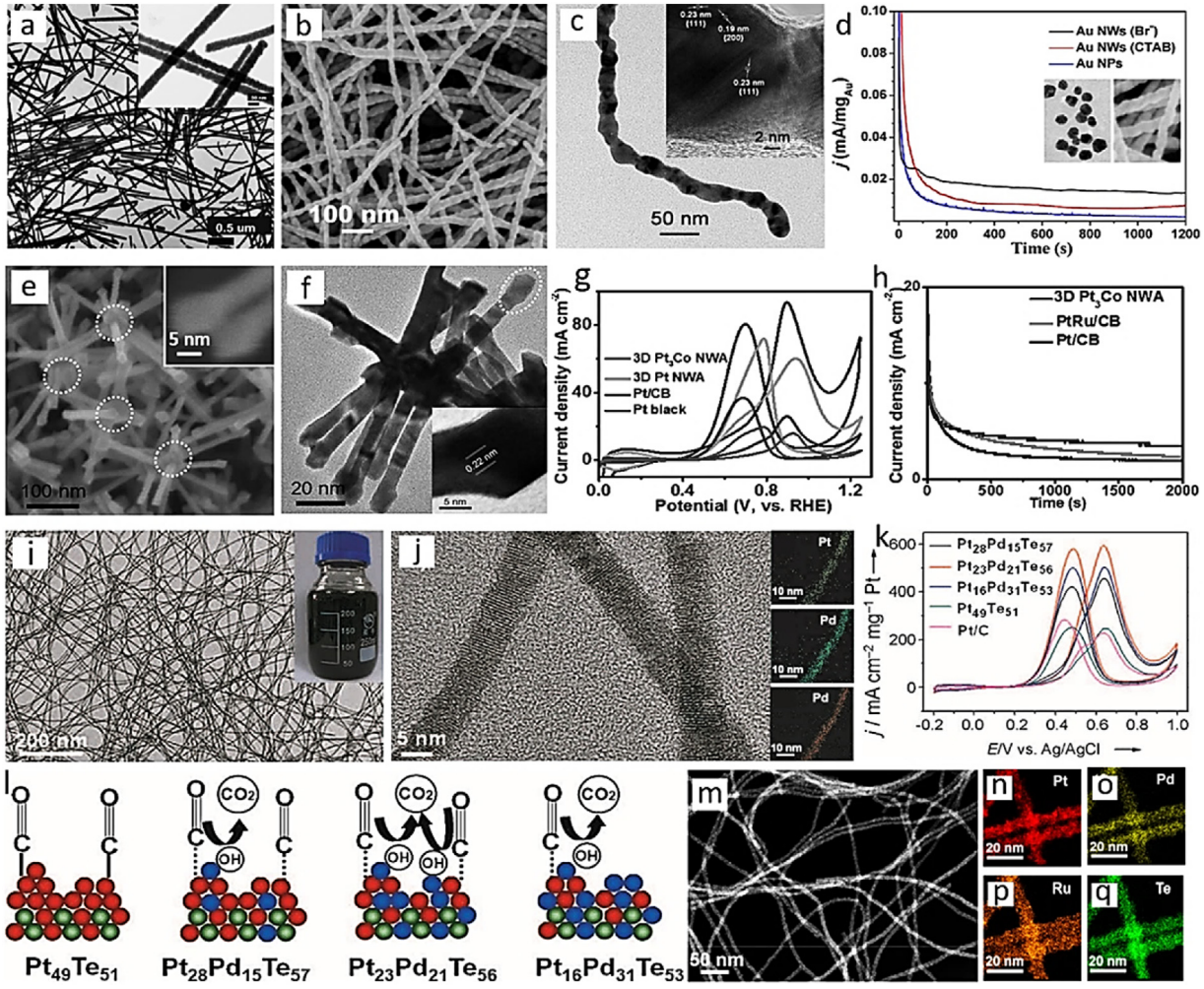

Fig. 2. (a) TEM image of the Pt NWs prepared from the PCTE membrane. *Inset* is the zoomed-in TEM image of the Pt NWs. (b) SEM and TEM (c) images of the Au NWs prepared by adding Te NWs into the aqueous solution of Au precursors. *Inset* in (c) is the HRTEM image of Au NWs. (d) Chronoamperometric curves of the Au NWs (Br^- and CTAB) and nanoparticles in Ar-saturated mixed solution of 1 M KOH and 1 M CH_3OH at 0.3 V. (e) SEM and TEM (f) images of the Pt_3Co NWs. (g) CV curves of the Pt_3Co and Pt NWs, Pt/CB and Pt black in 0.5 M H_2SO_4 + 0.5 M CH_3OH solution. (h) Chronoamperometric curves of the Pt_3Co and Pt NWs and Pt/CB electrocatalysts in 0.5 M H_2SO_4 + 0.5 M CH_3OH solution at 0.5 V. (i) TEM image of the $Pt_{23}Pd_{21}Te_{56}$ NWs. *Inset* in (i) is a photograph of an ethanol suspension of $Pt_{23}Pd_{21}Te_{56}$ NWs. (*j*) Enlarged TEM image and EDS mappings of the $Pt_{23}Pd_{21}Te_{56}$ NWs. (k) CV curves of the PtPdTe NWs, $Pt_{49}Te_{51}$ NWs, and Pt/C electrocatalysts for the MOR in 0.5 M H_2SO_4 + 1 M CH_3OH solution at 50 mVs^{-1}. (l) Illustration of the CO adsorbed on the $Pt_{49}Te_{51}$, $Pt_{28}Pd_{15}Te_{57}$, $Pt_{23}Pd_{21}Te_{56}$, and $Pt_{16}Pd_{31}Te_{53}$ NWs and the formation of Pd−OH at low potential to activate the oxidation of CO to generate CO_2. The bonding (dashed lines) of Pt−CO in PtPdTe NWs is weaker than that (solid lines) of Pt−CO in $Pt_{49}Te_{51}$ NWs due to the modified electronic structure of Pt. Red, blue, and green balls represent Pt, Pd, and Te atoms, respectively. The atom arrangement is in accordance with the atomic ratios of Pt/Te or Pt/Pd/Te NWs. (m–q) TEM image and energy dispersive X-ray (EDX) mappings of the $Pt_{17}Pd_{16}Ru_{22}Te_{45}$ NTs.
Source of a-d: Reproduced with permission from Ref. [95], © 2008 Elsevier; Source of e-h: Reproduced with permission from Ref. [104], © 2015 Wiley-VCH; Source of i-l: Reproduced with permission from Ref. [113], © 2013 Wiley-VCH; Source of m-q: Reproduced with permission from Ref. [114], © 2017 American Chemical Society.

oxygenous species. The introduction of Pd atoms facilitates the surface activity and stability of the quaternary PtPdRuTe NTs owing to the higher reduction potential and modified electronic structure of Pt. Benefiting from the above-mentioned advantages, the resultant quaternary PtPdRuTe NTs exhibited the enhanced catalytic activity and durability toward MOR when compared to the mono-, bi- and tri-metallic counterparts.

Although many literatures have been reported for the successful synthesis of 1D noble metal-based nanocrystals, most of them have a smooth surface and are enclosed with low energy crystal facets, which lead to underutilized activity. Manipulating the substructure of 1D noble metal-based nanocrystals to expose more active sites and high energy crystal facets through the shape engineering strategy is believed to be an effective method to achieve enhanced electrocatalytic performance [115–117]. The representative example is the wavy Pt multiple-twined NWs (MTNWs) prepared by Huang et al. (Fig. 3a) [118]. The change of growth direction contributes to the formation of zigzag and branch morphologies of Pt NWs, and abundant twin defects can be frequently found across the entire Pt NWs (Fig. 3b-f). The numerous twin defects and surface low-coordination atoms would potentially contribute to the enhancement of ORR activity. As a result, the Pt MTNWs display a higher mass activity of 0.144 mA μg^{-1} compared to the commercial Pt/C catalyst (0.091 mA μg^{-1}) (Fig. 3g). Similarly, Bu and co-workers reported a universal wet-chemical method for large-scale production of 1D multimetallic Pt-based catalysts with a high density of atomic steps [119]. Using bimetallic PtNi NWs as an example, they display high aspect ratio with the length of hundreds of nanometers and the diameter of about 10 nm and are intertwined to form networks (Fig. 3h). The XRD pattern and EDX spectrum confirm the formation of PtNi alloy NWs (Fig. 3i, *j*). The atomic structure of the 1D PtNi alloy catalysts was further revealed by the HRTEM image (Fig. 3k). It can be observed that the surface of the PtNi NWs is rough and numerous low-coordinate atomic steps, such as {211} and {311} steps exist on the outmost layer of NWs. The 1D PtNi NWs enclosed by a high density of atomic steps can

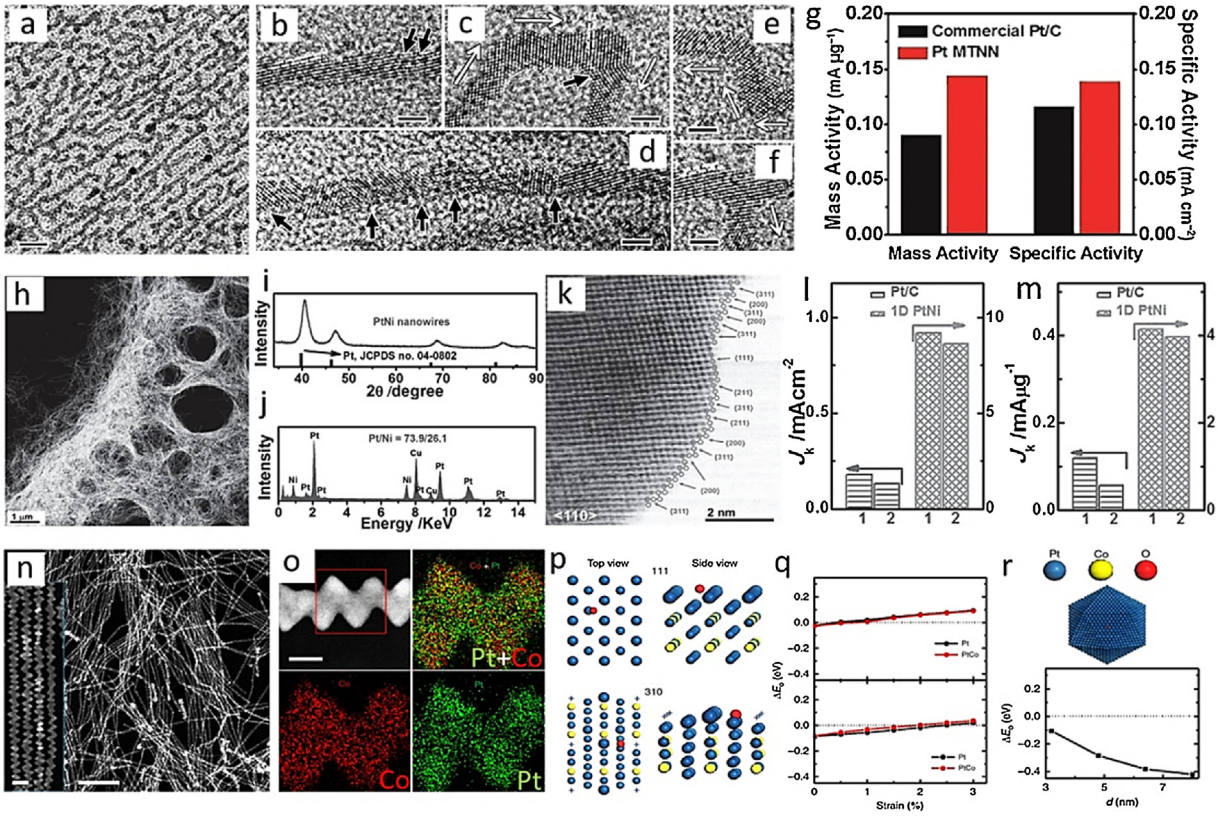

Fig. 3. (a) TEM and HRTEM (b–f) images of the Pt MTNWs. The scale bars are 10 (a) and 2 nm (b–f). (g) Mass and specific activities of the Pt MTNWs and commercial Pt/C catalysts toward ORR at 0.9 V. (h) High angle annular dark field image-scanning transmission electron microscope (HAADF-STEM) image of the PtNi NWs. (i) XRD pattern of the PtNi NWs. (*j*) EDX spectrum of the PtNi NWs. (k) HRTEM image of the PtNi NWs with high density of atomic steps. Changes of the specific (l) and mass (m) activities of the PtNi/C and commercial Pt/C catalysts in O_2-saturated 0.1 M $HClO_4$ before (1) and after (2) 10,000 cycles (scan rate: 50 mV s^{-1}). (n) HAADF-STEM image of the zigzag Pt_3Co NWs. The scale bars are 200 (n) and 20 nm (*inset* in n). (o) HAADF-STEM image and EDX mappings of the zigzag Pt_3Co NWs. The scale bar is 10 nm. (p, q) Atomic models of [110] and MRR-[310] surface and corresponding ΔE_O as a function of compressive strain. Blue cross represents the missing atomic row on the top layer of [310] surface. (r) ΔE_O on [111] facet of the Pt nanoparticles *versus* the particle size. The Pt nanoparticle was modeled by an icosahedron with 20 [111] facets.
Source of a-g: Reproduced with permission from Ref. [118], © 2013 Wiley-VCH; Source of h-m: Reproduced with permission from Ref. [119], © 2015 Wiley-VCH; Source of n-r: Reproduced with permission from Ref. [120], © 2016 Nature Publishing Group.

display excellent ORR specific and mass activities, which are 51.1 and 34.6 times higher than those of the commercial Pt/C catalysts, respectively (Fig. 3l, m).

Furthermore, the hierarchical zigzag ordered intermetallic Pt_3Co NWs enclosed with numerous step atoms were also synthesized using the similar wet-chemical approach (Fig. 3n, o) [120]. The hierarchical Pt_3Co NWs with a Pt-rich surface can display outstanding ORR performance with the mass and specific activities of 3.71 A mg^{-1}_{Pt} and 7.12 mA cm^{-2} at 0.9 V *vs.* RHE, which are 33.7 and 39.6 times higher than those of commercial Pt/C catalyst, respectively. Density functional theory (DFT) calculation was carried out to reveal the intrinsic mechanism of activity enhancement. It is found that the threefold hollow sites on the [110] and missrow reconstructed (MRR) [310] surfaces of the hierarchical Pt_3Co NWs are highly active for ORR (Fig. 3p, q). Their oxygen adsorption energy (ΔE_O) values *versus* compressive strain are much closer to zero than those of Pt nanoparticles (Fig. 3r). The compressive strain on both [110] and MRR-[310] facets could regulate the bonding of oxygen on the hierarchical Pt_3Co NWs, hence promoting the ORR performance.

1D core/shell noble metal-based electrocatalysts

Besides the alloying strategy, constructing core/shell architecture is also an effective approach to endow the 1D noble metal-based catalysts with high activity and durability. The core/shell nanostructure can greatly decrease the usage amount of active materials by decreasing the thickness of shell. In addition, the electrocatalytic properties of surface active materials on the 1D catalysts can be effectively tuned by the core materials *via* ligand and strain effects. Therefore, the selection of core materials is quite vital for the enhancement of electrocatalytic performance of the 1D core/shell noble metal-based nanocrystals. So far, various unitary noble metal, noble metal-based alloys, and non-noble metals have been extensively investigated as the 1D core materials to tailor the crystal lattice dimension and electronic structure of surface materials. For the single noble metals, 1D Pt, Pd and Au nanocrystals with stable physicochemical properties have been commonly used as the core materials in the core/shell nanostructures [121–123]. For example, recently, the crystal-phase-heterostructured 4 H/fcc Au/Pd core/shell NRs were synthesized using the template of 4 H/fcc Au NRs (Fig. 4a) [124]. The crystal-phase-heterostructured 4 H/fcc Au NRs were first prepared through a facile one-pot wet-chemical approach. After the reduction of H_2PdCl_4 in the presence of ascorbic acid (AA), the Pd shell epitaxially grows on the Au NRs (Fig. 4b). The obtained crystal-phase-heterostructured 4 H/fcc Au/Pd core/shell NRs display much higher electrocatalytic performance toward EOR than those of the commercial Pt/C and Pd black. The improved activity and stability could be attributed to the following reasons. First, the various coordination situation at the crystal boundaries could cause the difference of electronic structure, contributing to the improvement of electrocatalytic properties. Second, the rough surface of the Pd shell contains numerous atomic kinks and steps, which could also boost the activity. More importantly, the subsur-

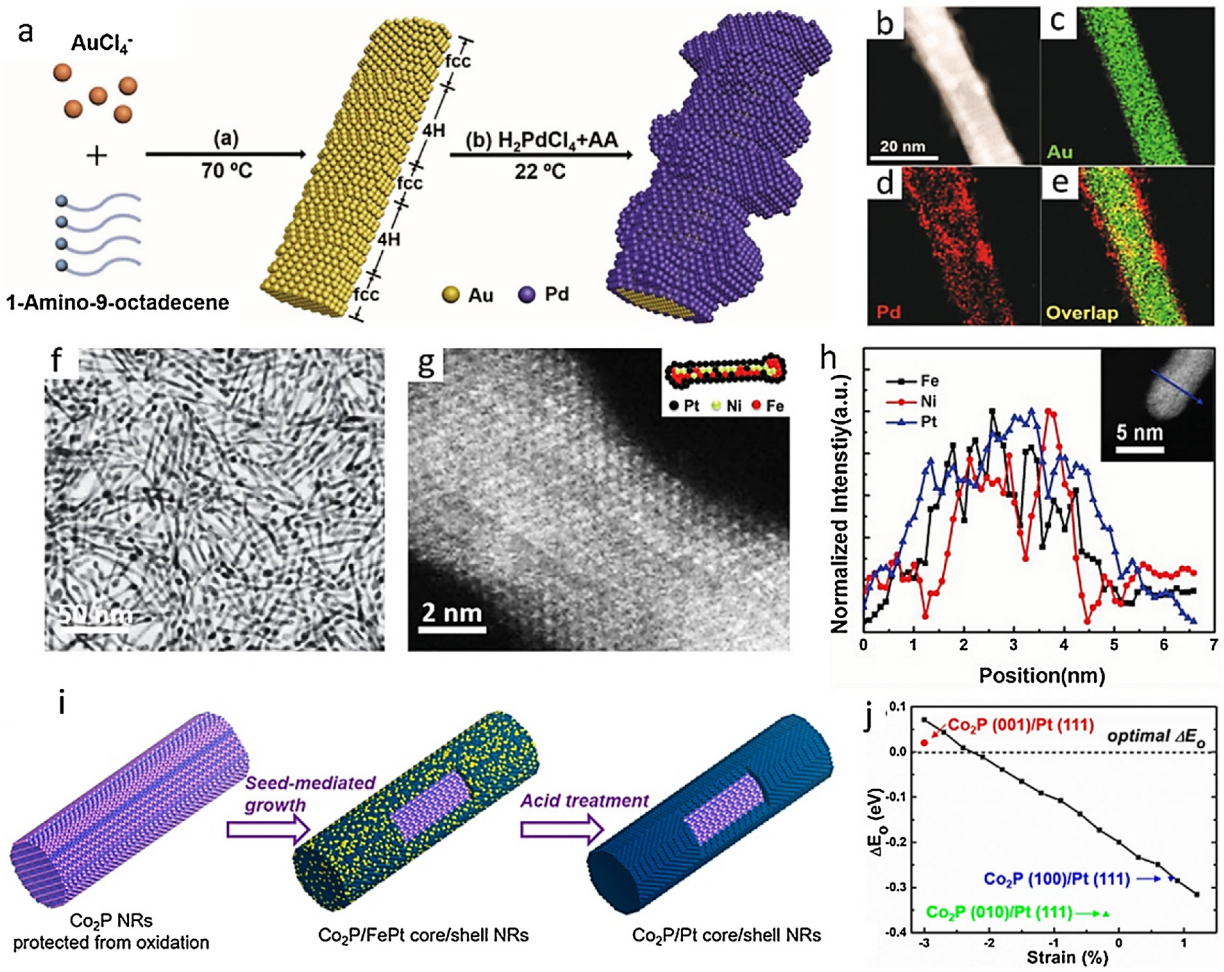

Fig. 4. (a) Schematic illustration of synthesis of the crystal-phase-heterostructured 4 H/fcc Au NRs and 4 H/fcc core/shell Au/Pd NRs. (b) HAADF-STEM image and (c–e) corresponding elemental mappings of the core/shell 4 H/fcc Au/Pd NRs. (f) TEM image of the core/shell FeNiPt/FePt NWs. HAADF-STEM image (g) and corresponding line-scan EELS spectra (h) of the core/shell FeNiPt/Pt NWs. (i) Schematic illustration of synthesis of the core/shell Co_2P/Pt NRs. (*j*) DFT calculations of various Co_2P/Pt interfaces. The negative and positive percent strain represent the compressive and tensile strain, respectively. The black curve displays the ΔE_O as a function of strain on the (111) surface of Pt. The green, blue, and red dots represent the ΔE_O for the Co_2P (010)/Pt (111), Co_2P (100)/Pt (111), and Co_2P (001)/Pt (111) interfaces, respectively.
Source of a-e: Reproduced with permission from Ref. [124], © 2017 Wiley-VCH; Source of f-h: Reproduced with permission from Ref. [129], © 2015 Wiley-VCH; Source of i-*j*: Reproduced with permission from Ref. [130], © 2018 American Chemical Society.

face 1D Au core can tune the electronic structure of surface Pd layer and stabilize Pd shell, and thus greatly enhance both the activity and stability.

Although the single noble metals, such as Pt, Pd and Au, are widely used as the core materials in 1D core/shell electrocatalysts, their cost is still too high in terms of commercialization. Thus, transition metals, such as Fe, Co, Ni, and Cu, can be alloyed with Pt, Pd, and Au to decrease the cost [125–128]. Especially, the lattice parameters of the core materials can be effectively manipulated through adjusting the ratio of noble and transition metals to optimize the electrocatalytic activity. For instance, Sun and co-workers reported core/shell FeNiPt/Pt NWs as a highly efficient catalyst toward ORR [129]. Fig. 4f shows the precursor of the as-synthesized FeNiPt/FePt core/shell NWs with a diameter of 4.5 ± 0.3 nm. After the AA treatment and annealing under 300 °C, the core/shell FeNiPt/FePt NWs were successfully transformed into FeNiPt/Pt NWs. Crystal boundaries can be obviously observed in the HAADF-STEM image, which indicates the formation of core/shell nanostructure (Fig. 4g). Line-scan electron energy loss spectroscopy (EELS) spectra further confirm the architectures of Pt shell and FeNiPt core (Fig. 4h). The subsurface Fe and Ni atoms in the core could induce lattice strain and electronic effects in the Pt shell, and thus optimize the oxygen binding energy of the surface Pt layer. As a result, the core/shell FeNiPt/Pt NWs exhibit superior specific and mass activities toward ORR, much higher than those of the ultrathin FeNiPt NWs and commercial Pt/C catalyst. Meanwhile, owing to the unique anisotropy of 1D nanostructure and the protection by Pt layer, the core/shell FeNiPt/Pt NWs display excellent durability with no apparent activity decay even after 10,000 CV cycles.

To completely avoid the use of noble metal-based core materials, the transition metal-based materials were recently proposed to serve as the effective core to construct the core/shell nanostructures. The representative example is the core/shell Co_2P/Pt NRs [130]. The core/shell Co_2P/Pt NRs were synthesized through facile seed-mediated growth and acid treatment (Fig. 4i). The Co_2P NRs with similar lattice constant with Pt was selected as the core materials for the epitaxial growth of ultrathin Pt shell ($\leq$1 nm). The researchers first conducted the DFT calculations to offer an in-depth and systematic understanding of the effects of Co_2P/Pt interfaces on the electrocatalytic activity of Pt shell toward ORR. Three models including Co_2P(010)/Pt(111), Co_2P(001)/Pt(111), and Co_2P(100)/Pt(111) interfaces have been established to calculate the surface ΔE_O (Fig. 4j). It can be seen that the point of Co_2P(100)/Pt(111) locates exactly on the black curve, revealing that the ΔE_O is dominated by the strain effect while the electronic effect is negligible. For the points of Co_2P(010)/Pt(111)

and $Co_2P(001)/Pt(111)$, both of them are located below the black curve, which indicates the electronic effect enhances the Pt-O bonding and causes the lower ΔE_O comparing with that predicted by strain effect. From the result, it can be concluded that the $Co_2P(001)/Pt(111)$ interface with the optimum ΔE_O value could possess the superior ORR activity due to the balance between strain and electronic effects, while the $Co_2P(010)/Pt(111)$ interface could be detrimental to ORR owing to the strong electronic effect. Inspired by the theoretical prediction, the Co_2P NRs mainly enclosed with (001) and (100) facets were successfully synthesized to construct the core/shell Co_2P/Pt NRs. As expected, the as-prepared Co_2P/Pt NRs exhibit high mass activity even after 10,000 cycles, still higher than the U.S. Department of Energy 2020 target (440 mA/mg_{Pt}). In addition, it should be pointed out that the composition and thickness of shell can also affect the respective contribution of electronic and strain effects at the core/shell interface, thus tune the electrocatalytic activity. To be specific, it is generally accepted that the strain effect is dominant when the thickness of Pt shell exceeds two or three atomic layers and becomes negligible when the thickness of Pt shell is larger than 1 nm [131]. As a result, the core/shell catalysts with one or two atomic Pt layer are most active toward ORR due to the synergy of strain and electronic effects.

1D heterogeneous noble metal-based electrocatalysts

In electrocatalysis, the heterojunctions in catalysts are often where the electrocatalytic reactions happen. Well-controlled heterogeneous noble metal-based nanocrystals have been demonstrated as effective electrocatalysts toward fuel-cell-related electrochemical energy conversion reactions. In general, there are three types of heterogeneous structures in the noble metal-based catalysts, including metal/organic molecule, metal/metal, and metal/metal compound. The host materials and foreign components should be rationally selected to regulate the electronic or steric effect for optimizing the electrocatalytic properties. Specifically, the integration of 1D nanostructure and heterojunctions in noble metal-based catalysts could further boost their activity and durability. Since the 1D noble metal-based catalysts equipped with the metal/organic molecule interface have been rarely reported, herein, we mainly focus on the 1D noble metal-based catalysts containing the interfaces of metal/metal and metal/metal compound. Until now, many studies have verified the metal/metal heterojunctions in noble metal-based catalysts are responsible for the enhancement of electrocatalytic performance [132,133]. Metal/metal heterojunctions on homogenous 1D catalysts are an ideal model for the study of interfacial effect. Given the significance of the interfacial effect in 1D noble metal-based catalysts, rationally constructing 1D heterogeneous catalysts with well-defined composition segregation and controllable interfacial structure *via* simple and scalable synthetic methods is highly desirable. Toward this end, Yu et al. designed heterogeneous Pt/PtTe NWs through a simple "precursor solution-aging" method [134]. The Pt nanoparticles with a diameter of 2–4 nm are homogenously decorated on the PtTe alloy NWs without agglomeration (Fig. 5a). The uniform distribution of ultrafine Pt nanoparticles on the surface of PtTe alloy NWs contributes to forming numerous available interfaces. Meanwhile, the *in-situ* anchoring of Pt nanoparticles on the PtTe alloy NWs can effectively prevent the coalescence and ripening of Pt nanoparticles. To elucidate the electronic effect enabled by the 1D heterogeneous Pt/PtTe nanostructure, the authors established two atomic models (PtTe NWs fully and partially covered by Pt) and carried out DFT calculations to investigate the interfacial charge distribution. The simulation results revealed that the work function of PtTe alloy (4.8 eV) is lower than that of the pure Pt (5.6 eV), which means free electrons can spontaneously transfer from the PtTe alloy NWs to Pt nanoparticles at the interface, thus, leading to interfacial charge polarization (Fig. 5b). Although the calculation results demonstrate the fewer charges being transferred to Pt nanoparticles in the partially covered PtTe NWs, its polarization effect is greatly stronger than that in the fully covered PtTe NWs when considering the size of ultrafine Pt nanoparticles (Fig. 5c and d). The strong interfacial polarization effect of the heterogenous Pt/PtTe NWs could help to improve oxygen adsorption and thus enhance the ORR activity. The experimental data further confirm the 1D heterogeneous $Pt/Pt_{51}Te_{49}$ NWs display the highest specific and mass activities compared with the homogenous $Pt_{48}Te_{52}$ alloy NWs and commercial Pt/C catalysts. Furthermore, the 1D heterogeneous $Pt/Pt_{51}Te_{49}$ NWs also exhibit much enhanced stability compared with the commercial Pt/C catalysts, which could be attributed to the interfacial stabilization. Similarly, some other 1D heterogeneous noble metal-based nanostructures, such as heterogeneous Pd/Au and Au/PtAu NTs, have been also successfully demonstrated and show excellent electrocatalytic performance [135,136].

Another typical heterojunction is the metal/metal compound interface. Depositing metal compounds with well-defined composition and size, such as metal oxides and sulfides, on various 1D noble metal-based nanocrystals is also an effective strategy to enhance the electrocatalytic activity. For examples, the 1D PtNi/NiS heterostructures were successfully synthesized through facilely sulfuring the composition-segregated Pt-Ni NWs (Fig. 5e) [137]. The ultrafine NiS nanocrystals intimately anchored on the PtNi NWs, forming a high density of well-defined PtNi/NiS interfaces (Fig. 5f). The interplanar crystal spacings derived from two different interfaces (region g and h) are 0.295 and 0.22 nm, corresponding to the (100) plane of NiS and (111) plane of Pt_3Ni, respectively (Fig. 5g and h). The optimized heterogeneous Pt_3Ni/NiS NWs exhibit outstanding HER activity in both alkaline and acid solution. Especially, the heterogeneous Pt_3Ni/NiS NWs display the highest activity toward HER in alkaline condition with a current density of 37.2 mA cm^{-2} at a low overpotential of 70 mV, 9.7 times higher than that of the commercial Pt/C catalyst. The interfacial effect at the PtNi/NiS heterojunctions was proposed to be the major factor for the enhancement of HER activity in alkaline condition, proved by the DFT calculations. It is generally believed that, for the HER in alkaline condition, the water dissociation is regarded as the key rate-determining step and promoting the cleavage of HO—H bond in the water molecules can enhance the kinetics of hydrogen evolution. According to the DFT results, the energy barrier of water dissociation on Pt (111) surface is as high as 0.89 eV, while the energy barrier of water dissociation on NiS (100) surface is decreased to 0.32 eV (Fig. 5i). The results indicate the NiS nanocrystals can dramatically accelerate water dissociation and promote the generation of adsorbed hydrogen atoms. Subsequently, the researchers calculated the free energy of hydrogen adsorption (G_{H^*}) on Pt (111), Pt_3Ni (111), and NiS (100) surfaces (Fig. 5j). It can be observed that the G_{H^*} on one of the two Pt_3Ni (111) is almost identical with that on the Pt (111) surface, while the G_{H^*} on NiS (100) surface is much stronger. Therefore, it can be concluded that the synergetic effect between the NiS for enhancing water dissolution and Pt_3Ni for optimizing H adsorption is responsible for the improvement of activity in alkaline condition for the 1D heterogeneous Pt_3Ni/NiS NWs. Similar studies on 1D heterogeneous noble metal-based nanocatalysts with metal/metal compound interfaces were also reported [138].

1D ultrathin noble metal-based electrocatalysts

Although 1D noble metal-based electrocatalysts with various nanostructures have been successfully demonstrated, the 1D nanocrystals with a large diameter still surfer from low atomic utilization. The 1D ultrathin architecture can maximize the surface-to-volume ratio and thus decrease the content of unavailable atoms

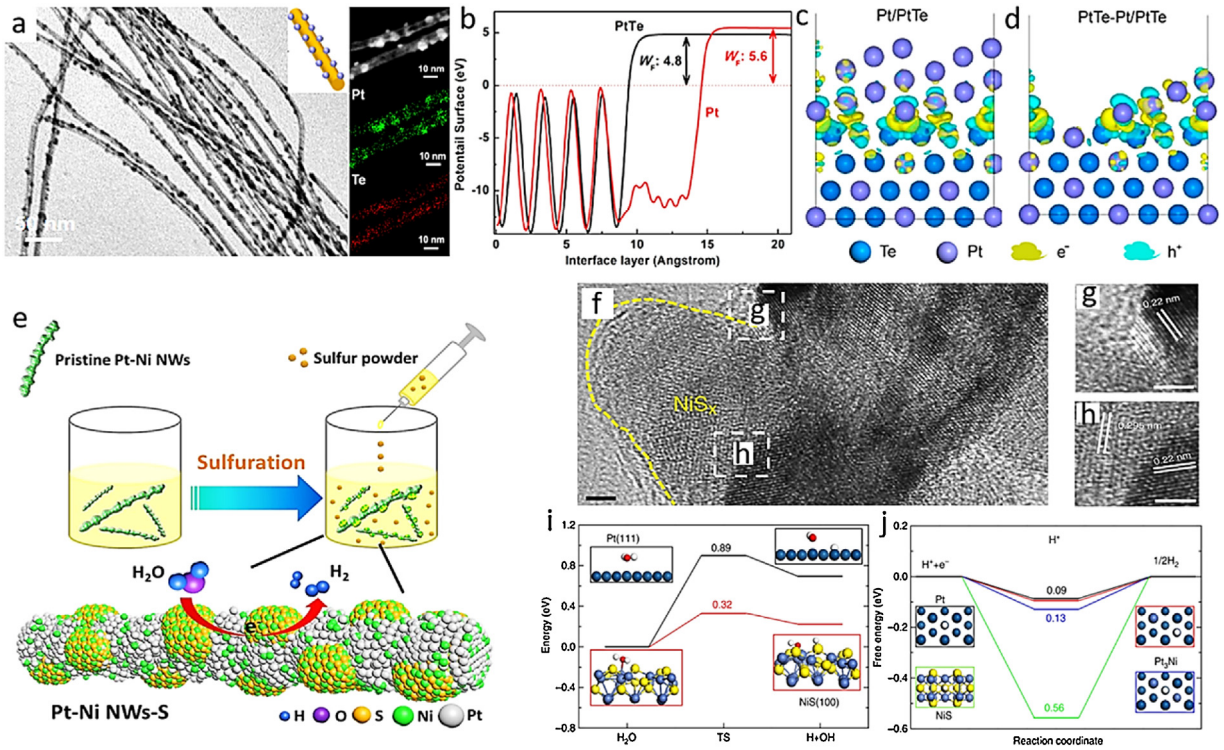

Fig. 5. (a) TEM image and corresponding elemental mappings of the heterogeneous Pt/PtTe MWs. (b) Calculated potential energy surface along the interface layer of the PtTe and Pt systems with (110) facets. Interface charge distribution of the PtTe NWs fully (c) and partially covered by Pt (d). (e) Schematic illustration showing the sulfuration of the PtNi NWs. (f–h) HRTEM images of the heterogeneous PtNi/NiS NWs. The scale bars are 2 nm (f–h). (i) Reaction energy diagram of water dissociation on the Pt (111) surface (black) and NiS (100) surface (red). (j) Free-energy barriers toward HER on the Pt (111) surface (black), Pt_3Ni (111) surface (red and blue) and NiS (100) surface (green) at U = 0 V. The red, white, yellow, dark blue and light blue spheres represent O, H, S, Pt and Ni atoms, respectively.
Source of a-d: Reproduced with permission from Ref. [134], © 2016 American Chemical Society; Source of e-j: Reproduced with permission from Ref. [137], © 2017 Nature Publishing Group.

inside the host materials. For instance, the ultrathin Rh-doped Pt NWs with a diameter of 1.3 nm possess an atomic utilization efficiency as high as 48.6% [139]. Such high utilization of atom can greatly improve the mass activity and reduce the usage of Pt. Especially, previously reported studies have verified that a surface contraction would occur on the NWs when the diameter is approximately smaller than 2 nm, and the intrinsic contraction stress can effectively tune the electrocatalytic activity [140]. Specifically, the surface contraction of Pt can weaken the bonding energy of oxygen and facilitate the formation of O—H bond, thus enhance the ORR activity. To avoid confusion, the 1D ultrathin noble metal-based electrocatalysts discussed here refer to the 1D nanocrystals with a diameter (or wall thickness) less than 2 nm. One of the most successful examples is the preparation of subnanometer Pt and Pt alloy NWs with 4–5 atomic layers (Fig. 6a) [141]. The electrochemically active surface area (ECSA) of the ultrathin Pt (76.4 $m^2 g^{-1}$), PtNi (80.7 $m^2 g^{-1}$), PtNiCo NWs (82.2 $m^2 g^{-1}$) is much higher than that of the Pt (4.5 nm) NWs (54.6 $m^2 g^{-1}$) and commercial Pt/C catalysts (69.3 $m^2 g^{-1}$). Furthermore, all the subnanometer Pt and Pt alloy NWs display greatly enhanced mass and specific capacities toward ORR compared with the commercial Pt/C catalyst (Fig. 6b and c). The superior activity of the ultrathin Pt alloy NWs is proposed to be attributed to the atomic thickness, (111)-terminated and Pt-rich surface. DFT calculations were further carried out to try to interpret the outstanding ORR performance of the subnanometer Pt-based NWs (Fig. 6d and e). The results show the ΔE_O on the (111) facet of the subnanometer Pt NWs is higher than that on the flat Pt (111) site, which is induced by the surface contraction strain of 1.5% on the (111) facet of the subnanometer Pt NWs. The surface compressive strain should be responsible for the enhanced ORR activity of the subnanometer Pt NWs. In addition, the simulation results also reveal the Ni atoms can relieve the undesirable over-binding between the ultrathin PtNi NWs and oxygen atoms, further promoting the ORR activity. Therefore, it can be concluded that the strain and electronic effects of the subnanometer Pt and Pt alloy NWs collectively boost the electrocatalytic performance toward ORR.

Apart from downsizing the diameter of 1D solid nanostructures, constructing 1D open and hollow NTs with an ultrathin wall is taken as another effective strategy to maximize the utilization efficiency of atoms. The representative example is the ultralong Pt NTs with an ultrathin wall (1 nm) [142]. Four Pt atom layers are deposited on Pd NWs with a diameter of 4.8 nm and subsequently etched away the Pd cores to form the ultrathin hollow Pt NTs (Fig. 6f). The HRTEM image exhibits the diameter and wall thickness of the ultrathin Pt NTs are $\approx 5.5 \pm 0.5$ and $\approx 1 \pm 0.2$ nm, respectively (Fig. 6g). According to the elemental mappings of the Pt NT, it can be observed that the Pt is uniformly distributed throughout the entire NTs. Meanwhile, the weak red signal indicates there is small amount of remnant Pd (2.55 wt%) in the final products of Pt NTs. Benefitting from the unique anisotropic 1D nanostructure and highly exposed Pt atoms, the Pt NTs display higher mass and specific activities than those of the Pd/Pt NWs and commercial Pt/C catalyst. Although the 1D ultrathin noble metal-based nanocrystals are a sort of promising electrocatalyst for fuel-cell-related electrochemical energy conversion reactions, the reliable, high-quality and scalable synthesis is still a great challenge that needs to be urgently addressed.

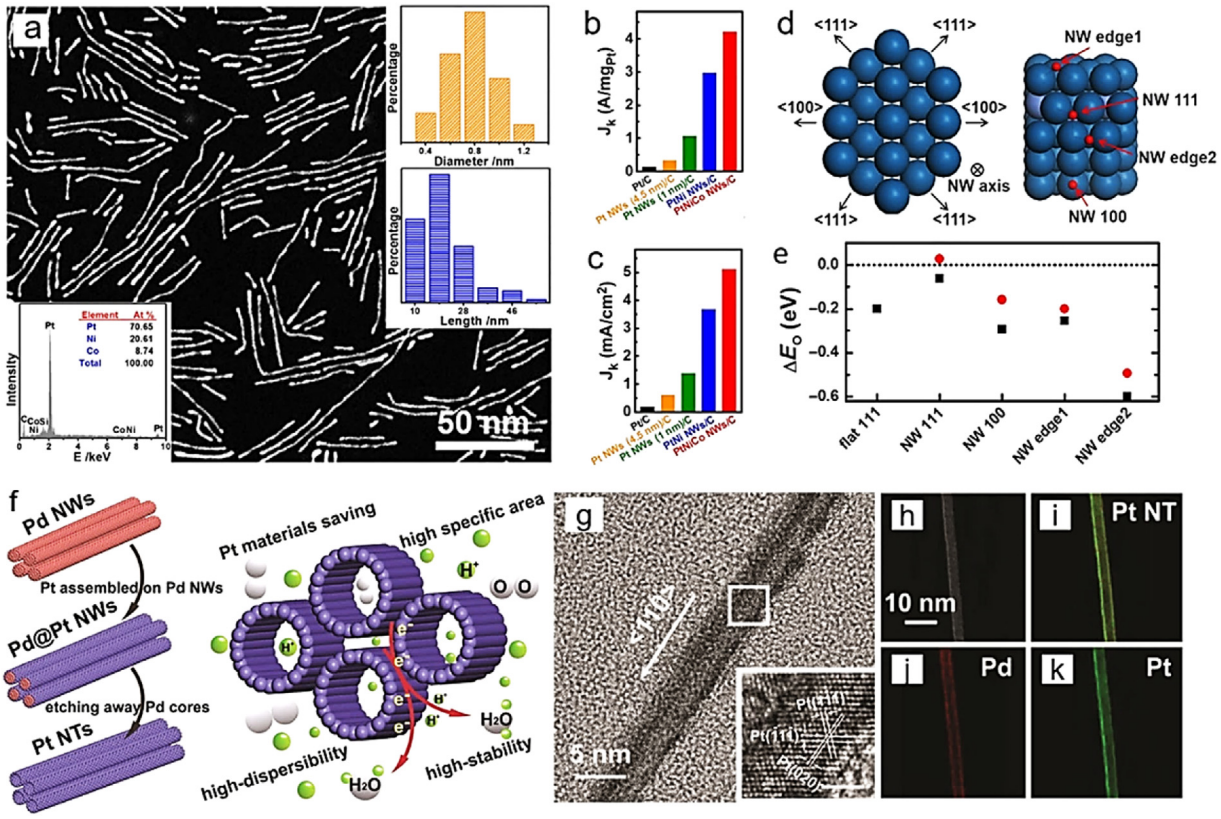

Fig. 6. (a) HAADF-STEM image of the subnanometer PtNiCo NWs. Left *inset* is the EDX spectrum of the subnanometer PtNiCo NWs. Right insets are the diameter and length distribution of the subnanometer PtNiCo NWs. Mass (b) and specific activities (c) of various catalysts toward ORR in an O_2-saturated 0.1 M $HClO_4$. (d) Atomic model showing the (111) and (100) facets and different O adsorption sites. Red ball represents O atom. (e) ΔE_O on various adsorption sites. Black square and red circle represent the ΔE_O on the pure Pt and PtNi NWs, respectively. The horizontal dotted line corresponds to the optimal ΔE_O. (f) Schematic illustration of the synthesis process of the Pt NTs with an ultrathin wall. (g) HRTEM image of the ultrathin Pt NTs. *Inset* is the enlarged view of the selected area. The scale bar in inset is 1 nm. (h–k) HAADF-TEM image and corresponding elemental mappings of the ultrathin Pt NTs.
Source of a-e: Reproduced with permission from Ref. [141], © 2017 Science; Source of f-k: Reproduced with permission from Ref. [142], © 2018 Wiley-VCH.

2D noble metal-based nanocrystals for electrocatalysis

2D unitary noble metal electrocatalysts

2D nanomaterials with unique anisotropic structure, high surface area and superior mechanical flexibility have also attracted much research interest in the field of electrochemical energy conversion during the past decades [143–146]. In particular, the emerging 2D non-layered noble metal-based nanocrystals have been intensively investigated recently as one of the most effective electrocatalysts toward various fuel-cell-related electrocatalysis [147]. The electrocatalytic properties of the 2D noble metal-based catalysts can be well regulated through manipulating the size, thickness, composition, and shape. Additionally, the 2D nanostructures with a high aspect ratio can act as ideal models to build the accurate structure-performance relationships and obtain comprehensive and in-depth understanding of the correlations between the preparation methods, microstructures, and intrinsic activities. For instance, the ultrathin truncated triangular Pt nanoplates (NPs) were synthesized using the galvanic-replacement-free epitaxial growth method (Fig. 7a) [148]. The ultrathin Pt NPs are single crystals and enclosed with exclusive {111} facets (Fig. 7b). From the cross-section TEM image, it can be observed that the thickness of the Pt layer is estimated to be $\tilde{2}$ nm (Fig. 7c). It is noted that the thickness and size of the ultrathin Pt NPs can be facilely tailored by controlling the time of seeded growth and using the different Ag NPs, respectively. Benefiting from the unique 2D nanostructure, the ultrathin Pt NPs exhibited much enhanced specific and mass activity toward ORR, which are $\tilde{2}2$ and $\tilde{9}.5$ times higher than those of the commercial Pt/C catalyst, respectively.

Pd is also a common *fcc* noble metal that has been successfully used for various catalysis, such as organic molecules electrooxidation and oxygen reduction. As a typical example, the high-quality ultrathin hexagonal Pd nanosheets (NSs) were synthesized based on the CO-confined growth strategy (Fig. 7d) [149]. In this method, the CO molecules are preferentially adsorbed on the (111) planes of Pd, which leads to the anisotropic growth and the formation of ultrathin 2D NSs. The appearance of 1/3(422) reflection in the selected area electron diffraction (SAED) pattern of Pd NSs further suggests that the exposure of (111) facet on the basal plane of ultrathin Pd NSs (Fig. 7e). In addition, it can be observed from the vertically aligned Pd NSs that the thickness mainly focuses at 1.8 nm, corresponding to about 10 atomic layers (Fig. 7f). The obtained Pd NSs display outstanding electrocatalytic activity toward FAOR, which is 2.5 times as active as that of the commercial Pd/C catalyst.

Ir and Ru are usually used as the benchmark electrocatalysts toward water oxidation and the 2D Ir and Ru nanocrystals have been successfully reported recently using the facile wet-chemical methods [150,151]. For example, the ultrathin Ru NSs with few hundred nanometers in size and 1–2 nm in thickness were prepared using the solvothermal approach (Fig. 7g) [152]. Owing to the high surface area and numerous accessible reactive sites, the ultrathin curled Ru NSs show much improved electrocatalytic performance toward water splitting compared with the Ru powder counterpart and commercial Pt/C catalyst in acid solution. As one of

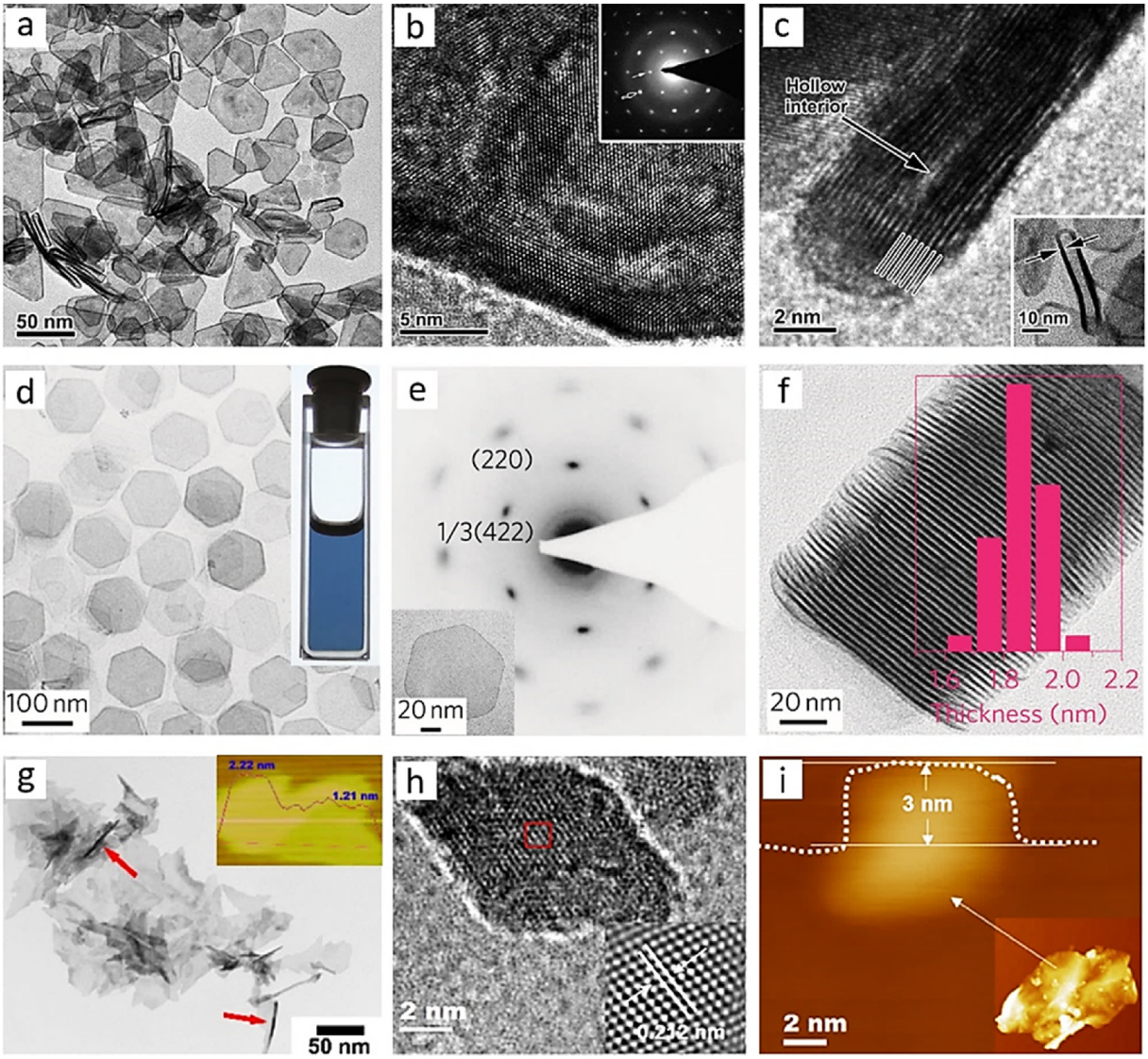

Fig. 7. TEM (a) and HRTEM (b) images of the ultrathin hollow Pt NPs. *Inset* in (b) is the SAED pattern of the ultrathin Pt NPs. (c) HRTEM image of a vertically aligned ultrathin Pt NP. *Inset* in (c) is the TEM image of a vertically aligned hollow Pt NP. (d) TEM image of the Pd NSs. *Inset*: photograph of an ethanol dispersion of the Pd NSs. (e) SAED pattern of a single Pd NS. (f) TEM image of the vertical Pd NSs. *Inset*: thickness distribution of the Pd NSs. (g) TEM image of the Ru NSs. *Inset*: AFM image of the ultrathin Ru NSs. (h) HRTEM image of the Rh NSs. (i) AFM images of the Rh NSs.
Source of a-c: Reproduced with permission from Ref. [148], © 2018 Royal Society of Chemistry;
Source of d-f: Reproduced with permission from Ref. [149], © 2011 Nature Publishing Group;
Source of g: Reproduced with permission from Ref. [152], © 2016 American Chemical Society; Source of h-i: Reproduced with permission from Ref. [154], © 2017 American Chemical Society.

the noble metals, the Rh is even rarer than Pt. Constructing ultrathin 2D nanostructure contributes to decreasing the utilization amount and promoting the activity and stability [153]. Recently, a one-pot hydrothermal method was developed for the synthesis of Rh NSs exposed with (111) plane on reduced graphene oxide (RGO) (Fig. 7h) [154]. The atomic force microscopy (AFM) image reveals the thickness of the Rh NSs is about 3 nm (Fig. 7i). The newly developed Rh-NSs/RGO hybrid exhibits superior electrocatalytic activity toward MOR in alkaline solution, much better than Rh nanoparticles and Rh nanoparticles-RGO composite.

2D binary and polynary noble metal alloy electrocatalysts

Although the ultrathin 2D monometallic nanocrystals with high surface-to-volume ratio and high densities of exposed atoms display favorable electrocatalytic performance, their activity and durability can be further enhanced by the formation of metallic alloy [155–157]. For instance, the ultrathin Pd NSs exhibit better electrocatalytic activity compared to the concave tetrahedral Pd nanocrystal and commercial Pd/C catalyst, but their poisoning tolerance to intermediates, such as CO, urgently needs to be improved [158]. To this end, ultrathin PdCu alloy NSs with thickness of 2.8 ± 0.3 nm were synthesized by the co-reduction of palladium acetylacetonate and copper acetylacetonate in the presence of molybdenum hexacarbonyl (Fig. 8a) [159]. XPS results display the red shift of the Pd $3d_{5/2}$ and Pd $3d_{3/2}$ of PdCu alloy NSs, suggesting the modified electronic structure of Pd in PdCu alloy NSs (Fig. 8b). The EDX images further reveal homogenous distribution of Pd and Cu in the NSs (Fig. 8c). As a result, the optimized ultrathin PdCu NSs exhibit much enhanced catalytic performance toward FAOR compared with the commercial Pd/C catalyst. The improved electrocatalytic activity of the PdCu alloy NSs is mainly attributed to the 2D ultrathin nanostructure and the synergistic effect between Pd and Cu atoms.

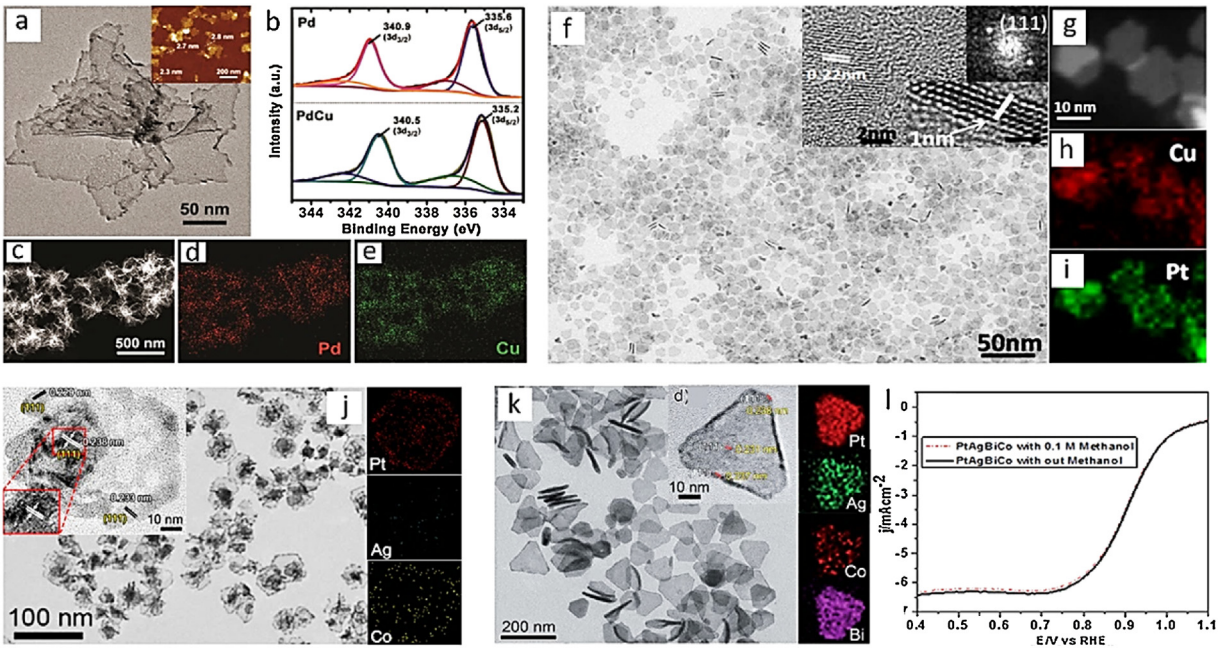

Fig. 8. (a) TEM image of the ultrathin PdCu NSs. (b) XPS spectra of Pd 3d in Pd and PdCu NSs. HAADF-STEM image (c) and EDX mappings (d, e) of the PdCu NSs. (f) TEM image of the ultrathin PtCu NSs. *Inset* in (f) is the HRTEM image of the ultrathin PtCu NSs. Bottom right of inset showing the thickness of the ultrathin PtCu NSs. Top right of *inset* is the fast Fourier transform (FFT) pattern of the PtCu NSs. (g–i) HAADF-STEM image and EDX mappings of the PtCu NSs. (*j*) TEM image and EDX mappings of the PtAgCo NSs. *Inset*: HRTEM image of the PtAgCo NSs. (k) TEM image and EDX mappings of the PtAgBiCo NPs. *Inset*: HRTEM image of the PtAgBiCo NPs. (l) ORR polarization curves of the PtAgBiCo/C electrocatalyst in a O_2-saturated 0.1 M $HClO_4$ solution with and without 0.1 M methanol.
Source of a-e: Reproduced with permission from Ref. [159], © 2017 Wiley-VCH; Source of f-i: Reproduced with permission from Ref. [162], © 2013 American Chemical Society; Source of *j*: Reproduced with permission from Ref. [163], © 2017 American Chemical Society; Source of k-l: Reproduced with permission from Ref. [164], © 2017 Royal Society of Chemistry.

To date, Pt is still the only choice in modern fuel-cell technology. Unfortunately, the rarity and high cost of Pt greatly hinder their further widespread applications. The aim for the high-performance fuel cell is to design highly active and stable electrocatalysts with low Pt utilization amounts. An effective strategy to address this problem is to construct ultrathin 2D Pt-M (M = transition metals) alloy nanostructure [160,161]. However, the 2D alloy nanostructures are more usually found in the limited noble metals such as Ag, Au and Pd, and the 2D Pt-based alloys remain understudied. The high-quality ultrathin PtCu alloy NSs with an adjustable size of basal plane from 8 to 50 nm were prepared through a two-step method (Fig. 8f) [162]. In the synthesis, the gel system was formed in the first step and used for confining the nucleation and growth of alloy nanocrystals in the second reduction process. The thickness of the PtCu NSs is controlled to be about 1 nm, corresponding to 5–6 atomic layers (inset in Fig. 8f). The elemental mappings reveal both Pt and Cu are homogenously distributed on the 2D nanocrystals and the Cu to Pt atomic ratio is estimated to be 2:1 based on the EDX spectrum and ICP results. Owing to the abundant active sites of 2D nanostructure and the optimized electronic structure of Pt, the ultrathin PtCu NSs display the exceptional electrocatalytic activity and stability toward EOR.

Using the similar two-step synthetic method, the ultrathin ternary PtAgCo alloy NSs were successfully synthesized, which exhibit excellent electrocatalytic activity toward HER (Fig. 8j) [163]. They found that the incorporation of Ag contributes to the formation of 2D morphology, and the Co can result in downshift of the d-band centers of Pt and decrease the adsorption of H atoms on Pt, accelerating the HER process. Based on the ultrathin 2D ternary alloy system, Bi atoms were further introduced into the ternary alloy matrix, producing the tetrametallic PtAgBiCo NPs for ORR (Fig. 8k) [164]. The incorporation of Bi can enhance the resistivity of the PtAgBiCo alloy toward methanol poisoning caused by methanol crossover in a direct methanol fuel cell (DMFC) (Fig. 8l).

2D core/shell noble metal-based electrocatalysts

By integrating the unique 2D morphology and core/shell nanostructure, the 2D core/shell noble metal-based electrocatalysts display excellent electrocatalytic performance toward various renewable energy conversion reactions [165–168]. A monolayer or a few layers of noble metal atoms covered on the less expensive 2D core materials can effectively decease the utilization amounts of target noble metals. More importantly, the electrocatalytic properties of the 2D core/shell nanocrystals can be effectively regulated by the match between core and shell materials, owing to the structure-induced ligand and strain effects. For example, the ultrathin core/shell Pd/$Pt_{monolayer}$ NPs were synthesized using the modified defect-mediated thin-film growth method (Fig. 9a) [169]. The ultrathin Pd NPs with a thickness of 5 nm were first obtained *via* a facile colloidal method in the presence of CO (Fig. 9b). Subsequently, a uniform monolayer of Pt atom was electrodeposited on the Pd NPs by cycling the electrochemical potential (Fig. 9c). The obtained core/shell Pd/$Pt_{monolayer}$ NPs achieved superior specific and mass activity toward ORR, which are 3.4 and 6.6 times higher than those of the commercial Pt/C catalyst, respectively. The enhanced electrocatalytic activity toward ORR can be attributed to the enhanced Pt utilization and optimized oxygen affinity on Pt shell induced by Pd core.

For the 2D core/shell nanostructures, their electrocatalytic performance can be further boosted by the shell engineering. For instance, it is generally believed that the pure Pt shell is vulnerable to the poisoned CO generated in MOR. To address this problem, the core/shell Pd/PtM (M = Ni, Rh, Ru) NPs with adjustable thickness

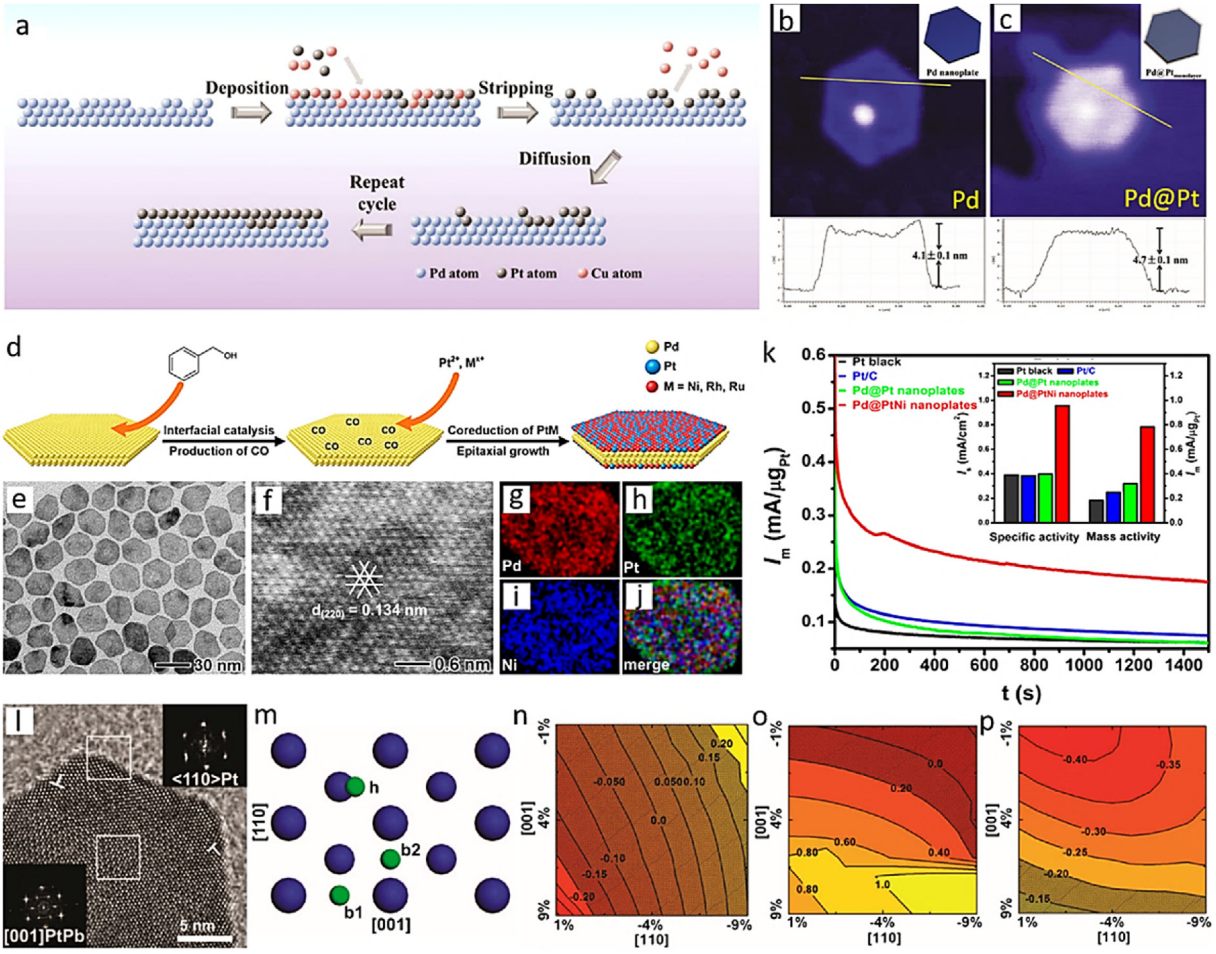

Fig. 9. (a) Schematic illustration of the formation of Pd/$Pt_{monolayer}$ NPs. AFM images of the pure Pd (b) and Pd/$Pt_{monolayer}$ NPs (c) with height details. (d) Schematic illustration of the epitaxial growth of the core/shell Pd/PtM (M = Ni, Rh, Ru) NPs. TEM (e) and HRTEM images (f) of the Pd/PtNi NPs. (g–j) EDX mappings of the Pd/PtNi NPs. (k) Current-time curves of various catalysts toward MOR at 0.85 V *vs.* RHE for 1500s. *Inset*: mass and specific activities of various catalysts toward MOR. (l) HRTEM image of single hexagonal PtPb NPs. *Inset*: FFT patterns from the white squares at the edge and inside of the PtPb NPs. (m) Atomic model of the Pt (110) surface. Three O adsorption sites: hollow ("h") and two bridge sites ("b1″ and "b2″). Blue and green balls represent Pt and O atoms, respectively. ΔE_O as a function of biaxial strain in [110] and [001] directions for the "h" (n) and "b1″ (o), and "b2″ sites (p).

Source of a-c: Reproduced with permission from Ref. [169], © 2015 Royal Society of Chemistry; Source of d-k: Reproduced with permission from Ref. [170], © 2016 American Chemical Society; Source of l-p: Reproduced with permission from Ref. [171], © 2016 Science.

were synthesized *via* a facile and universal method [170]. In the synthesis, the *in-situ* formation of CO at the surface of Pd nanosheets is the key factor to generate the well-defined core/shell Pd/PtM (M = Ni, Rh, Ru) NPs (Fig. 9d). The *in-situ* generated CO adsorbed on Pd NPs not only acts as the reducing agent to accelerate the reduction of Pt and other transition metals, but also decrease the surface energy of Pt-based alloy shell through the strong adsorption. TEM image in Fig. 9e shows a typical core/shell Pd/PtNi NPs with a good morphology uniformity. The HAADF-STEM image of the core/shell Pd/PtNi NPs display a lattice distance of 0.134 nm, corresponding to the {220} facet of PtNi or Pd alloy (Fig. 9f). Moreover, the EDX mappings of the ultrathin Pd/PtNi NPs reveal homogenous distribution of Pd, Pt and Ni atoms, indicating the formation of core/shell multimetallic nanostructure (Fig. 9g-*j*). The ultrathin core/shell Pd/PtNi NPs display the enhanced activity and stability compared to the core/shell Pd/Pt NPs, Pt black, and commercial Pt/C (Fig. 9k). The great catalytic activity enhancement was proposed to be ascribed to the 2D core/shell nanostructure (high active sites), electronic coupling (Pd can weaken the adsorption of CO on Pt) and bifunctional mechanism (oxyphilic Ni facilitates the formation of OH and removal of adsorbed CO on Pt).

Rationally designing the core materials to manipulate the electrocatalytic performance of 2D core/shell architectures is another effective strategy for various electrochemical energy conversion reactions. Recently, a new class of hexagonal core/shell PtPb/Pt NPs were demonstrated to be extremely active toward ORR [171]. The hexagonal core/shell PtPb/Pt NPs possess a thickness of 4.5 nm and an edge length of 16 nm. The HRTEM image reveals some dislocations between the edge and the interior around the corners, contributing to releasing the mismatching strain (Fig. 9l). The FFT patterns show a hexagonal phase in the inner plane and a cubic phase at the edge, which confirm the formation of core/shell nanostructure (*inset* in Fig. 9l). Electrochemical results display the mass and specific activity of the hexagonal core/shell PtPb/Pt NPs can be as high as 4.3 A mg^{-1} and 7.8 mA cm^{-2} at 0.9 V *vs.* RHE, respectively. To get in-depth insights on the exceptional ORR performance of the hexagonal core/shell PtPb/Pt NPs, DFT simulations were conducted for the calculation of the ΔE_O. Two types of interfacial planes were formed in the PtPb nanoplates: {010}PtPb//{110}Pt between the PtPb and the edge-Pt layer, and {001}PtPb//{110}Pt between PtPb and top (bottom)-Pt layer. Moreover, the SAED and HRTEM results reveal a large tensile strain along [001] and a compressive strain along [110] on both the top-Pt and edge-Pt surfaces of the nanoplates. Therefore, the ΔE_O was calculated on the Pt (110) surface as a function of strain along the [110] and [001] directions (Fig. 9m–p). The results indicate the "h" and

"b2″ sites under biaxial strains are responsible for the high ORR activity.

2D heterogeneous noble metal-based electrocatalysts

Heterogeneous nanomaterials based on noble metals are expected to exhibit high activity for various electrocatalytic reactions. It is generally believed that the heterojunctions with different crystal structures and electron states can induce the strain and electronic effects. These changes would tune the electrocatalytic performance by changing the adsorption of reactants and intermediates on the surface of catalysts. Specifically, the 2D heterogeneous noble metal-based nanostructures have gradually aroused the researchers' interest recently due to the unique 2D morphology and well-defined interface structure. Although the 2D heterogeneous noble metal-based nanocrystals possess a great potential for different electrocatalysis, the investigation in 2D heterogeneous noble metal-based electrocatalysts is still in the early stage, awaiting the controllable method for the synthesis of heterojunctions with well-defined size and morphology. As a typical example, the 2D Pt-Pd bimetallic heterostructures were constructed using a facile seed-mediated method [172]. The Pd NSs were first synthesized with the basal plane enclosed by (111) facets and side plane covered by (100) facets. Subsequently, the Pt nanocrystals were selectively deposited on the basal and side planes of Pd NSs with and without using the CTAB, respectively (Fig. 10a). Since the morphology, size, and crystal facets of the Pt nanoparticles on the two different models are same, the difference of electrocatalytic properties between the two heterogeneous systems could be solely resulted from the different interfacial structures. The DFT calculations were carried out to investigate the electronic interactions at the interfaces of Pd(100)-Pt and Pd(111)-Pt (Fig. 10b and c). The results indicate the charge redistribution oscillations at the interfacial region and the chemical bonding at the interface of Pd(100)-Pt is stronger than that of the Pd(111)-Pt. As a result, the 2D heterogeneous Pd-Pt-S nanocrystals with numerous interfaces of Pd(100)-Pt exhibit much higher activity toward MOR and EOR compared to those of the commercial Pd/C, Pt/C, Pd NSs, and Pd-Pt-T catalysts (Fig. 10d–f). This work offered a promising strategy to synthesize highly active electrocatalysts through engineering the interfaces.

Apart from the noble metal-noble metal interfaces, constructing noble metal-transition metal heterojunctions is also a promising

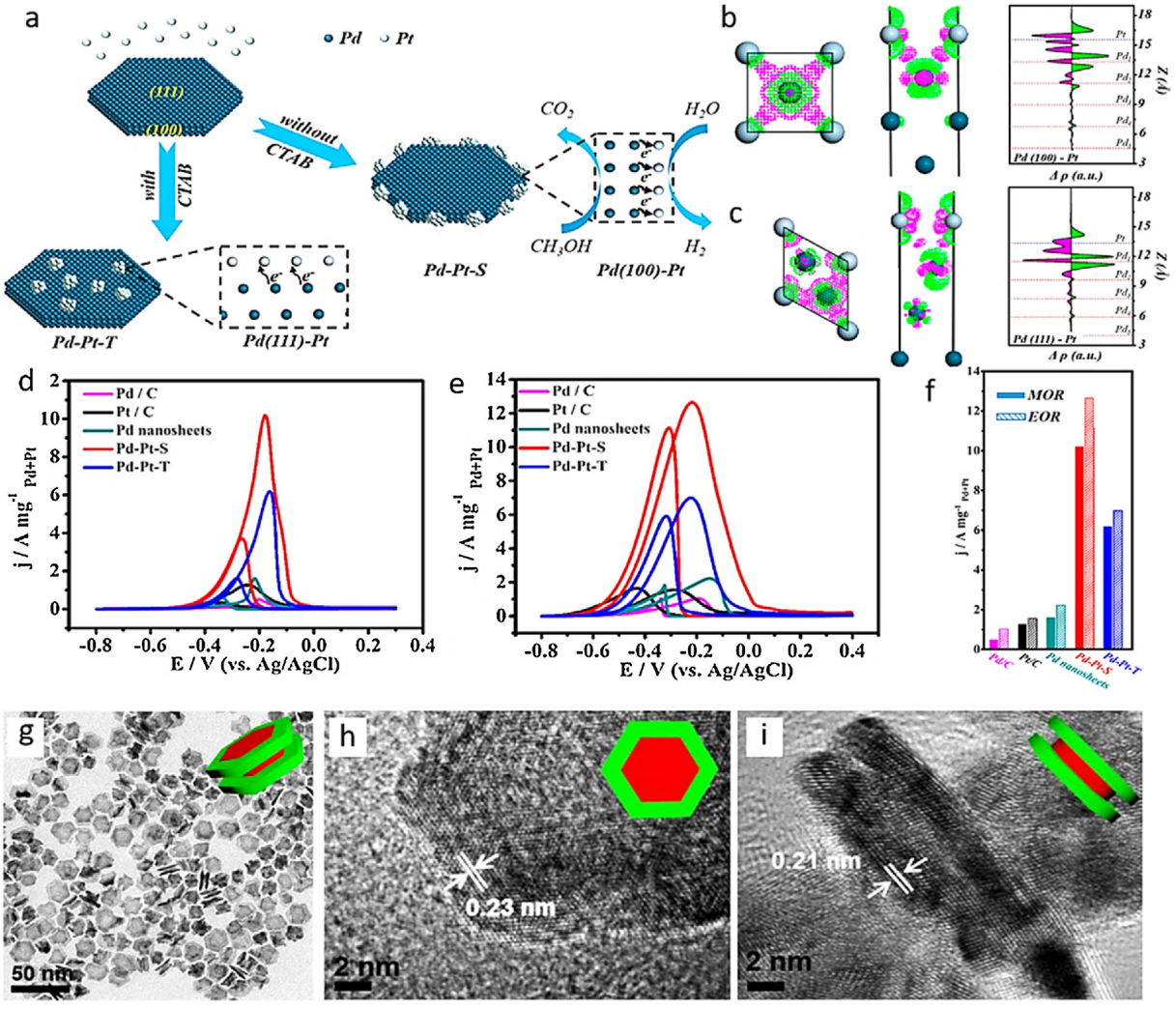

Fig. 10. (a) Schematic illustration of the heterogeneous PdPt NPs in the absence and presence of CTAB. (b) Top and side views of charge difference and corresponding plane-averaged electron density difference along the direction perpendicular to the interface of Pd(100)-Pt model. (c) Top and side views of charge difference and corresponding plane-averaged electron density difference along the direction perpendicular to the interface of Pd(111)-Pt model. CV curves of various catalysts toward MOR (d) and EOR (e). (f) Mass activities of various catalysts toward MOR and EOR. (g) TEM image of the sandwiched Ru_2Ni_2 NPs. HRTEM images of the top (h) and side (i) views of the sandwiched Ru_2Ni_2 NPs.

Source of a-f: Reproduced with permission from Ref. [172], © 2017 American Chemical Society; Source of g-i: Reproduced with permission from Ref. [173], © 2018 Elsevier.

strategy that can not only decrease the utilization amount of noble metals, but also boost the electrocatalytic performance. In this regard, recently, a unique sandwich-like Ru-Ni heterostructure was synthesized, of which two hexagonal Ru rings were covered on the ends of a Ni pillar (Fig. 10g–i) [173]. The optimized heterogeneous sandwiched Ru_2Ni_2 NPs with abundant interfaces display high HER activity with a low overpotential of 40 mV at 10 mA cm^{-2} and a small Tafel slope of 23 mV dec^{-1} in a 1 M KOH solution. More importantly, the heterogeneous sandwiched Ru_2Ni_2 NPs exhibit superior electrocatalytic performance toward overall water splitting with a low onset potential of 1.45 V and excellent stability in a 1 M KOH solution, which can be potentially applied in the practical alkaline electrolysis.

Conclusions and perspectives

In recent years, constructing 1D and 2D noble metal-based nanocatalysts has exhibited enormous potential for enhancing the electrocatalytic properties toward various fuel-cell-related electrocatalysis. In this review, we have presented the major advances in 1D and 2D noble metal-based electrocatalysts in terms of nanoarchitecture engineering and their potential electrocatalytic applications. Especially, the underlying structure-related mechanisms were detailly revealed and are expected to offer a guidance for the rational design of 1D and 2D noble metal-based electrocatalysts. Although much progress has been made, it remains many challenges and further concerns should be focused on the following aspects.

First, there are still some technological problems needed to be solved to realize the controllable and scalable preparation of 1D and 2D noble metal-based nanocatalysts. To date, the 1D and 2D noble metal-based nanocrystals are usually synthesized using the wet-chemical methods, in which the organic solvents and surfactants are always involved. The removal of organic solvents and surfactants inevitably increase the cost and operation complexity. In addition, due to the high anisotropy of 1D and 2D nanostructures, it is a great challenge to precisely control the growth kinetics to obtain the high-yield and high-quality nanocrystals. Therefore, much effort is urgently needed to develop facile and effective strategies to synthesize 1D and 2D noble metal-based nanocrystals with desired nanostructures on a large scale and at low cost.

Secondly, the redox reactions occur at the interface between solid catalysts and solution during electrocatalysis. The surface of catalysts, especially for the thermodynamically unstable 1D and 2D noble metal-based nanocrystals, usually undergoes structural evolutions under the complex electrochemical environments. The lack of valid characterization techniques for real-time recording the change of surface structure greatly impedes the identification of real active sites. Developing advanced *in-situ* characterization techniques, such as *in-situ* FTIR and *in-situ* XAFS, can offer the realistic data for the structural changes during electrocatalysis, which contributes to establishing accurate atomic models and revealing the intrinsic structure-activity-relationship.

Thirdly, in-depth understandings of the interaction between the atomic structures and properties help to design highly active 1D and 2D noble metal-based catalysts. Despite great developments have been obtained in the theoretical simulations, such as DFT calculation, there are still large differences between the simulated models and realistic systems at present. The simplified electrochemical environments in the simulated models usually cannot comprehensively and exactly reflect the real conditions. Therefore, developing advanced theoretical simulation technology can not only accurately explain and forecast the structure-property-relationship, but also provide guidance to construct ideal electrocatalysts.

Last but not the least, although standard three-electrode systems are a favorable platform to investigate the kinetics and intrinsic activity of electrocatalysts, the obtained data lack practical device relevance. Some important factors affecting the performance of fuel-cell-related devices (fuel cells and water electrolysis), such as mass transfer, heat and water management, and ion transport, need not be considered in the three-electrode tests using ultrathin films of active materials. Therefore, in the future, it is highly encouraged to evaluate the electrochemical performance of 1D and 2D noble metal-based electrocatalysts in realistic full-cell devices.

Acknowledgments

We are grateful for the financial support of this work from the Beijing Natural Science Foundation (JQ18005), the National Key R&D Program of China (2016YFB0100201), the National Natural Science Foundation of China (51671003) and the Young Thousand Talented Program. We also acknowledge the financial support of the Initiative Postdocs Supporting Program (BX20180001) and the China Postdoctoral Science Foundation (2018M640024).

References

[1] Z.W. Seh, J. Kibsgaard, C.F. Dickens, I. Chorkendorff, J.K. Nørskov, T.F. Jaramillo,Science 355 (2017), eaad4998.
[2] H. Mistry, A.S. Varela, S. Kuehl, P. Strasser, B.R. Cuenya, Nat. Rev. Mater. 1 (2016) 16009.
[3] N.M. Markovic, Nat. Mater. 12 (2013) 101.
[4] X. Liu, L. Dai, Nat. Rev. Mater. 1 (2016) 16064.
[5] J. Tang, J. Liu, N.L. Torad, T. Kimura, Y. Yamauchi, Nano Today 9 (2014) 305–323.
[6] Y. Li, T. Gao, Y. Yao, Z. Liu, Y. Kuang, C. Chen, J. Song, S. Xu, E.M. Hitz, B. Liu,Adv. Energy Mater. 8 (2018), 1801289.
[7] Y. He, X. Zhuang, C. Lei, L. Lei, Y. Hou, Y. Mai, X. Feng, Nano Today 24 (2019) 103–119.
[8] K. Qu, Y. Zheng, X. Zhang, K. Davey, S. Dai, S.Z. Qiao, ACS Nano 11 (2017) 7293–7300.
[9] Y. Han, Y.-G. Wang, W. Chen, R. Xu, L. Zheng, J. Zhang, J. Luo, R.-A. Shen, Y. Zhu, W.-C. Cheong, J. Am. Chem. Soc. 139 (2017) 17269–17272.
[10] J. Zhang, L. Dai, ACS Catal. 5 (2015) 7244–7253.
[11] F.-L. Meng, Z.-L. Wang, H.-X. Zhong, J. Wang, J.-M. Yan, X.-B. Zhang, Adv. Mater. 28 (2016) 7948–7955.
[12] K.N. Dinh, Q. Liang, C.-F. Du, J. Zhao, A.I.Y. Tok, H. Mao, Q. Yan, Nano Today (2019) 99–121.
[13] C. Meng, T. Ling, T.Y. Ma, H. Wang, Z. Hu, Y. Zhou, J. Mao, X.W. Du, M. Jaroniec, S.Z. Qiao,Adv. Mater. 29 (2017), 1604607.
[14] S. Dou, X. Wang, S. Wang,Small Methods 3 (2019), 1800211.
[15] Y. Wang, B. Kong, D. Zhao, H. Wang, C. Selomulya, Nano Today 15 (2017) 26–55.
[16] H. Osgood, S.V. Devaguptapu, H. Xu, J. Cho, G. Wu, Nano Today 11 (2016) 601–625.
[17] H. Jin, X. Liu, A. Vasileff, Y. Jiao, Y. Zhao, Y. Zheng, S.-Z. Qiao, ACS Nano 12 (2018) 12761–12769.
[18] Q. Yun, Q. Lu, X. Zhang, C. Tan, H. Zhang, Angew. Chemie Int. Ed. 57 (2018) 626–646.
[19] Q. Gao, W. Zhang, Z. Shi, L. Yang, Y. Tang,Adv. Mater. 31 (2019), 1802880.
[20] W.T. Hong, M. Risch, K.A. Stoerzinger, A. Grimaud, J. Suntivich, Y. Shao-Horn, Energy Environ. Sci. 8 (2015) 1404–1427.
[21] Y. Kang, P. Yang, N.M. Markovic, V.R. Stamenkovic, Nano Today 11 (2016) 587–600.
[22] S. Sui, X. Wang, X. Zhou, Y. Su, S. Riffat, C.-j. Liu, J. Mater. Chem. A Mater. Energy Sustain. 5 (2017) 1808–1825.
[23] Y.-J. Wang, N. Zhao, B. Fang, H. Li, X.T. Bi, H. Wang, Chem. Rev. 115 (2015) 3433–3467.
[24] L. Li, L. Hu, J. Li, Z. Wei, Nano Res. 8 (2015) 418–440.
[25] K. Jukk, N. Kongi, P. Rauwel, L. Matisen, K. Tammeveski, Electrocatalysis 7 (2016) 428–440.
[26] Q. Shao, K. Lu, X. Huang,Small Methods 3 (2019), 1800545.
[27] K. Jiang, Q. Shao, D. Zhao, L. Bu, J. Guo, X. Huang,Adv. Funct. Mater. 27 (2017), 1700830.
[28] X.L. Tian, Y.Y. Xu, W. Zhang, T. Wu, B.Y. Xia, X. Wang, ACS Energy Lett. 2 (2017) 2035–2043.
[29] H. Jin, C. Guo, X. Liu, J. Liu, A. Vasileff, Y. Jiao, Y. Zheng, S.-Z. Qiao, Chem. Rev. 118 (2018) 6337–6408.
[30] J. Liu, D. Zhu, Y. Zheng, A. Vasileff, S.-Z. Qiao, ACS Catal. 8 (2018) 6707–6732.

[31] A. Yu, C. Lee, N.-S. Lee, M.H. Kim, Y. Lee, ACS Appl. Mater. Inter. 8 (2016) 32833–32841.
[32] W. Huang, X. Kang, C. Xu, J. Zhou, J. Deng, Y. Li, S. Cheng,Adv. Mater. 30 (2018), 1706962.
[33] X. Qiu, H. Zhang, P. Wu, F. Zhang, S. Wei, D. Sun, L. Xu, Y. Tang,Adv. Funct. Mater. 27 (2017), 1603852.
[34] L. Figueroa-Cosme, Z.D. Hood, K.D. Gilroy, Y. Xia, J. Mater. Chem. C Mater. Opt. Electron. Devices 6 (2018) 4677–4682.
[35] H. Yin, S. Zhao, K. Zhao, A. Muqsit, H. Tang, L. Chang, H. Zhao, Y. Gao, Z. Tang, Nat. Commun. 6 (2015) 6430.
[36] D.Y. Chung, J.M. Yoo, Y.E. Sung,Adv. Mater. 30 (2018), 1704123.
[37] H. Lv, Y. Wang, A. Lopes, D. Xu, B. Liu, Appl. Catal. B 249 (2019) 116–125.
[38] Q.-Q. Fu, H.-H. Li, S.-Y. Ma, B.-C. Hu, S.-H. Yu, Sci. China Mater. 59 (2016) 112–121.
[39] J. Lai, S. Guo,Small 13 (2017), 1702156.
[40] F. Muench, Catalysts 8 (2018) 597.
[41] G. Wang, S. Tao, Y. Liu, L. Guo, G. Qin, K. Ijiro, M. Maeda, Y. Yin, Chem. Commun. (Camb.) 52 (2016) 398–401.
[42] Y. Pei, L. Huang, J. Wang, L. Han, S. Li, S. Zhang, H. Zhang,Nanotechnology 30 (2019), 222001.
[43] X. Yan, Y. Chen, S. Deng, Y. Yang, Z. Huang, C. Ge, L. Xu, D. Sun, G. Fu, Y. Tang, Chem. - Eur. J. 23 (2017) 16871–16876.
[44] L. Wang, Z. Zeng, W. Gao, T. Maxson, D. Raciti, M. Giroux, X. Pan, C. Wang, J. Greeley, Science 363 (2019) 870–874.
[45] M.E. Scofield, Y. Zhou, S. Yue, L. Wang, D. Su, X. Tong, M.B. Vukmirovic, R.R. Adzic, S.S. Wong, ACS Catal. 6 (2016) 3895–3908.
[46] H.-H. Li, S.-Y. Ma, Q.-Q. Fu, X.-J. Liu, L. Wu, S.-H. Yu, J. Am. Chem. Soc. 137 (2015) 7862–7868.
[47] S. Guo, D. Li, H. Zhu, S. Zhang, N.M. Markovic, V.R. Stamenkovic, S. Sun, Angew. Chemie Int. Ed. 52 (2013) 3465–3468.
[48] X. Huang, Y. Chen, C.-Y. Chiu, H. Zhang, Y. Xu, X. Duan, Y. Huang, Nanoscale 5 (2013) 6284–6290.
[49] C. Gao, Q. Zhang, Z. Lu, Y. Yin, J. Am. Chem. Soc. 133 (2011) 19706–19709.
[50] Z. Fan, Z. Luo, X. Huang, B. Li, Y. Chen, J. Wang, Y. Hu, H. Zhang, J. Am. Chem. Soc. 138 (2016) 1414–1419.
[51] Y. Gong, X. Liu, Y. Gong, D. Wu, B. Xu, L. Bi, L.Y. Zhang, X. Zhao, J. Colloid Interface Sci. 530 (2018) 189–195.
[52] G. Fu, X. Jiang, M. Gong, Y. Chen, Y. Tang, J. Lin, T. Lu, Nanoscale 6 (2014) 8226–8234.
[53] B.Y. Xia, H.B. Wu, Y. Yan, X.W. Lou, X. Wang, J. Am. Chem. Soc. 135 (2013) 9480–9485.
[54] H. Wang, X. He, Y. Zhao, J. Li, T. Huang, H. Liu, CrystEngComm 19 (2017) 4304–4311.
[55] X. Liu, L. Li, Y. Yang, Y. Yin, C. Gao, Nanoscale 6 (2014) 4513–4516.
[56] W.-C. Cheong, C. Liu, M. Jiang, H. Duan, D. Wang, C. Chen, Y. Li, Nano Res. 9 (2016) 2244–2250.
[57] X. Yin, Q. Chen, P. Tian, P. Zhang, Z. Zhang, P.M. Voyles, X. Wang, Chem. Mater. 30 (2018) 3308–3314.
[58] Y. Li, W. Wang, K. Xia, W. Zhang, Y. Jiang, Y. Zeng, H. Zhang, C. Jin, Z. Zhang, D. Yang, Small 11 (2015) 4745–4752.
[59] Z. Liu, X. Yang, B. Lu, Z. Shi, D. Sun, L. Xu, Y. Tang, S. Sun, Appl. Catal. B 243 (2019) 86–93.
[60] F. Saleem, B. Xu, B. Ni, H. Liu, F. Nosheen, H. Li, X. Wang, Adv. Mater. 27 (2015) 2013–2018.
[61] L. Dai, S. Mo, Q. Qin, X. Zhao, N. Zheng, Small 12 (2016) 1572–1577.
[62] J. Ge, P. Wei, G. Wu, Y. Liu, T. Yuan, Z. Li, Y. Qu, Y. Wu, H. Li, Z. Zhuang, Angew. Chemie Int. Ed. 57 (2018) 3435–3438.
[63] X. Fu, Z. Zhao, C. Wan, Y. Wang, Z. Fan, F. Song, B. Cao, M. Li, W. Xue, Y. Huang, Nano Res. 12 (2019) 211–215.
[64] K. Jiang, L. Bu, P. Wang, S. Guo, X. Huang, ACS Appl. Mater. Inter. 7 (2015) 15061–15067.
[65] V. Stamenkovic, B.S. Mun, K.J. Mayrhofer, P.N. Ross, N.M. Markovic, J. Rossmeisl, J. Greeley, J.K. Nørskov, Angew. Chemie Int. Ed. 45 (2006) 2897–2901.
[66] D. Wang, Y. Yu, H.L. Xin, R. Hovden, P. Ercius, J.A. Mundy, H. Chen, J.H. Richard, D.A. Muller, F.J. DiSalvo, Nano Lett. 12 (2012) 5230–5238.
[67] K.A. Kuttiyiel, K. Sasaki, Y. Choi, D. Su, P. Liu, R.R. Adzic, Nano Lett. 12 (2012) 6266–6271.
[68] S. Rudi, D. Teschner, V. Beermann, W. Hetaba, L. Gan, C. Cui, M. Gliech, R. Schlögl, P. Strasser, ACS Catal. 7 (2017) 6376–6384.
[69] Q. Jia, K. Caldwell, K. Strickland, J.M. Ziegelbauer, Z. Liu, Z. Yu, D.E. Ramaker, S. Mukerjee, ACS Catal. 5 (2014) 176–186.
[70] C. Wang, M. Chi, G. Wang, D. Van der Vliet, D. Li, K. More, H.H. Wang, J.A. Schlueter, N.M. Markovic, V.R. Stamenkovic, Adv. Funct. Mater. 21 (2011) 147–152.
[71] C. Wang, D. Van Der Vliet, K.L. More, N.J. Zaluzec, S. Peng, S. Sun, H. Daimon, G. Wang, J. Greeley, J. Pearson, Nano Lett. 11 (2010) 919–926.
[72] C. Cui, L. Gan, H.-H. Li, S.-H. Yu, M. Heggen, P. Strasser, Nano Lett. 12 (2012) 5885–5889.
[73] F. Lima, J. Zhang, M. Shao, K. Sasaki, M. Vukmirovic, E. Ticianelli, R. Adzic, J. Phys. Chem. C 111 (2007) 404–410.
[74] C. Roth, A. Papworth, I. Hussain, R. Nichols, D. Schiffrin, J. Electroanal. Chem. 581 (2005) 79–85.
[75] Z. Liu, G.S. Jackson, B.W. Eichhorn, Angew. Chemie Int. Ed. 49 (2010) 3173–3176.
[76] W. Du, G. Yang, E. Wong, N.A. Deskins, A.I. Frenkel, D. Su, X. Teng, J. Am. Chem. Soc. 136 (2014) 10862–10865.
[77] B. Lim, M. Jiang, P.H. Camargo, E.C. Cho, J. Tao, X. Lu, Y. Zhu, Y. Xia, Science 324 (2009) 1302–1305.
[78] V.R. Stamenkovic, B.S. Mun, K.J. Mayrhofer, P.N. Ross, N.M. Markovic, J. Am. Chem. Soc. 128 (2006) 8813–8819.
[79] C. Wang, M. Chi, D. Li, D. Strmcnik, D. Van der Vliet, G. Wang, V. Komanicky, K.-C. Chang, A.P. Paulikas, D. Tripkovic, J. Am. Chem. Soc. 133 (2011) 14396–14403.
[80] B.-W. Zhang, Z.-C. Zhang, H.-G. Liao, Y. Gong, L. Gu, X.-M. Qu, L.-X. You, S. Liu, L. Huang, X.-C. Tian, Nano Energy 19 (2016) 198–209.
[81] C.-H. Cui, S.-H. Yu, Acc. Chem. Res. 46 (2013) 1427–1437.
[82] K. Shin, L. Zhang, H. An, H. Ha, M. Yoo, H.M. Lee, G. Henkelman, H.Y. Kim, Nanoscale 9 (2017) 5244–5253.
[83] Y.P. Zhu, C. Guo, Y. Zheng, S.-Z. Qiao, Acc. Chem. Res. 50 (2017) 915–923.
[84] B. Wu, N. Zheng, Nano Today 8 (2013) 168–197.
[85] Z. Liu, J. Qi, M. Liu, S. Zhang, Q. Fan, H. Liu, K. Liu, H. Zheng, Y. Yin, C. Gao, Angew. Chemie. 130 (2018) 11852–11856.
[86] C. Meng, T. Ling, T.Y. Ma, H. Wang, Z. Hu, Y. Zhou, J. Mao, X.W. Du, M. Jaroniec, S.Z. Qiao,Adv. Mater. 29 (2017), 1604607.
[87] C.-H. Cui, J.-W. Yu, H.-H. Li, M.-R. Gao, H.-W. Liang, S.-H. Yu, ACS Nano 5 (2011) 4211–4218.
[88] J. Yang, L. Qiu, B. Liu, Y. Peng, F. Yan, S. Shang, J. Polym. Sci. Part A: Polym. Chem. 49 (2011) 4531–4538.
[89] H.W. Liang, X. Cao, F. Zhou, C.H. Cui, W.J. Zhang, S.H. Yu, Adv. Mater. 23 (2011) 1467–1471.
[90] Q. Lu, A.L. Wang, H. Cheng, Y. Gong, Q. Yun, N. Yang, B. Li, B. Chen, Q. Zhang, Y. Zong,Small 14 (2018), 1801090.
[91] X. Huang, S. Li, S. Wu, Y. Huang, F. Boey, C.L. Gan, H. Zhang, Adv. Mater. 24 (2012) 979–983.
[92] J.-J. Feng, D.-L. Zhou, H.-X. Xi, J.-R. Chen, A.-J. Wang, Nanoscale 5 (2013) 6754–6757.
[93] L. Fu, F. Yang, G. Cheng, W. Luo, Nanoscale 10 (2018) 1892–1897.
[94] B.R. Sathe, B.K. Balan, V.K. Pillai, Energy Environ. Sci. 4 (2011) 1029–1036.
[95] S.M. Choi, J.H. Kim, J.Y. Jung, E.Y. Yoon, W.B. Kim, Electrochim. Acta 53 (2008) 5804–5811.
[96] T. Guo, G. Yu, Y. Zhang, H. Xiang, F. Chang, C.-J. Zhong, J. Phys. Chem. C 121 (2017) 3108–3116.
[97] C. Wang, Y. Hou, J. Kim, S. Sun, Angew. Chemie Int. Ed. 46 (2007) 6333–6335.
[98] H.-H. Li, Q.-Q. Fu, L. Xu, S.-Y. Ma, Y.-R. Zheng, X.-J. Liu, S.-H. Yu, Energy Environ. Sci. 10 (2017) 1751–1756.
[99] H. Lv, X. Chen, D. Xu, Y. Hu, H. Zheng, S.L. Suib, B. Liu, Appl. Catal. B 238 (2018) 525–532.
[100] W. Liu, D. Haubold, B. Rutkowski, M. Oschatz, R. Hübner, M. Werheid, C. Ziegler, L. Sonntag, S. Liu, Z. Zheng, Chem. Mater. 28 (2016) 6477–6483.
[101] F. Chang, S. Shan, V. Petkov, Z. Skeete, A. Lu, J. Ravid, J. Wu, J. Luo, G. Yu, Y. Ren, J. Am. Chem. Soc. 138 (2016) 12166–12175.
[102] P. Wu, H. Zhang, Y. Qian, Y. Hu, H. Zhang, C. Cai, J. Phys. Chem. C 117 (2013) 19091–19100.
[103] Y. Zeng, Z. Shao, H. Zhang, Z. Wang, S. Hong, H. Yu, B. Yi, Nano Energy 34 (2017) 344–355.
[104] B.Y. Xia, H.B. Wu, N. Li, Y. Yan, X.W. Lou, X. Wang, Angew. Chemie Int. Ed. 54 (2015) 3797–3801.
[105] C.-H. Cui, H.-H. Li, S.-H. Yu, Chem. Sci. 2 (2011) 1611–1614.
[106] H.-Y. Park, J.H. Park, P. Kim, S.J. Yoo, Appl. Catal. B 225 (2018) 84–90.
[107] X.X. Du, Y. He, X.X. Wang, J.N. Wang, Energy Environ. Sci. 9 (2016) 2623–2632.
[108] C. Jung, C. Lee, K. Bang, J. Lim, H. Lee, H.J. Ryu, E. Cho, H.M. Lee, ACS Appl. Mater. Inter. 9 (2017) 31806–31815.
[109] S. Maksimuk, S. Yang, Z. Peng, H. Yang, J. Am. Chem. Soc. 129 (2007) 8684–8685.
[110] L. Liu, E. Pippel, Angew. Chemie Int. Ed. 50 (2011) 2729–2733.
[111] H.-H. Li, C.-H. Cui, S. Zhao, H.-B. Yao, M.-R. Gao, F.-J. Fan, S.-H. Yu, Adv. Energy Mater. 2 (2012) 1182–1187.
[112] M.E. Scofield, C. Koenigsmann, L. Wang, H. Liu, S.S. Wong, Energy Environ. Sci. 8 (2015) 350–363.
[113] H.H. Li, S. Zhao, M. Gong, C.H. Cui, D. He, H.W. Liang, L. Wu, S.H. Yu, Angew. Chemie Int. Ed. 52 (2013) 7472–7476.
[114] S.-Y. Ma, H.-H. Li, B.-C. Hu, X. Cheng, Q.-Q. Fu, S.-H. Yu, J. Am. Chem. Soc. 139 (2017) 5890–5895.
[115] N. Zhang, L. Bu, S. Guo, J. Guo, X. Huang, Nano Lett. 16 (2016) 5037–5043.
[116] M. Luo, Y. Sun, X. Zhang, Y. Qin, M. Li, Y. Li, C. Li, Y. Yang, L. Wang, P. Gao,Adv. Mater. 30 (2018), 1705515.
[117] X. Huang, Z. Zhao, Y. Chen, C.-Y. Chiu, L. Ruan, Y. Liu, M. Li, X. Duan, Y. Huang, Nano Lett. 14 (2014) 3887–3894.
[118] L. Ruan, E. Zhu, Y. Chen, Z. Lin, X. Huang, X. Duan, Y. Huang, Angew. Chemie Int. Ed. 52 (2013) 12577–12581.
[119] L. Bu, J. Ding, S. Guo, X. Zhang, D. Su, X. Zhu, J. Yao, J. Guo, G. Lu, X. Huang, Adv. Mater. 27 (2015) 7204–7212.
[120] L. Bu, S. Guo, X. Zhang, X. Shen, D. Su, G. Lu, X. Zhu, J. Yao, J. Guo, X. Huang, Nat. Commun. 7 (2016) 11850.
[121] Q. Lu, A.-L. Wang, Y. Gong, W. Hao, H. Cheng, J. Chen, B. Li, N. Yang, W. Niu, J. Wang, Nat. Chem. (2018) 1.
[122] Y.L. Zhang, W.J. Shen, W.T. Kuang, S. Guo, Y.J. Li, Z.H. Wang, ChemSusChem 10 (2017) 2375–2379.

[123] N. Zhang, S. Guo, X. Zhu, J. Guo, X. Huang, Chem. Mater. 28 (2016) 4447–4452.
[124] Y. Chen, Z. Fan, Z. Luo, X. Liu, Z. Lai, B. Li, Y. Zong, L. Gu, H. Zhang,Adv. Mater. 29 (2017), 1701331.
[125] N. Zhang, Y. Feng, X. Zhu, S. Guo, J. Guo, X. Huang,Adv. Mater. 29 (2017), 1603774.
[126] S. Guo, S. Zhang, D. Su, S. Sun, J. Am. Chem. Soc. 135 (2013) 13879–13884.
[127] L.X. Ding, G.R. Li, Z.L. Wang, Z.Q. Liu, H. Liu, Y.X. Tong, Chem. - Eur. J. 18 (2012) 8386–8391.
[128] C. Koenigsmann, S.S. Wong, Energy Environ. Sci. 4 (2011) 1161–1176.
[129] H. Zhu, S. Zhang, D. Su, G. Jiang, S. Sun, Small 11 (2015) 3545–3549.
[130] C. Liu, Z. Ma, M. Cui, Z. Zhang, X. Zhang, D. Su, C.B. Murray, J.X. Wang, S. Zhang, Nano Lett. 18 (2018) 7870–7875.
[131] M. Luo, S. Guo, Nat. Rev. Mater. 2 (2017) 17059.
[132] Z. Peng, H. Yang, J. Am. Chem. Soc. 131 (2009) 7542–7543.
[133] R. Xie, S. Lu, Y. Deng, S. Mei, X. Cao, L. Zhou, C. Lan, H. Gu, Inorg. Chem. (2019), http://dx.doi.org/10.1021/acs.inorgchem.8b03321.
[134] H.-H. Li, M.-L. Xie, C.-H. Cui, D. He, M. Gong, J. Jiang, Y.-R. Zheng, G. Chen, Y. Lei, S.-H. Yu, Chem. Mater. 28 (2016) 8890–8898.
[135] K. Cai, J. Liu, H. Zhang, Z. Huang, Z. Lu, M.F. Foda, T. Li, H. Han, Chem. - Eur. J. 21 (2015) 7556–7561.
[136] K. Cai, Y. Liao, H. Zhang, J. Liu, Z. Lu, Z. Huang, S. Chen, H. Han, ACS Appl. Mater. Inter. 8 (2016) 12792–12797.
[137] P. Wang, X. Zhang, J. Zhang, S. Wan, S. Guo, G. Lu, J. Yao, X. Huang, Nat. Commun. 8 (2017) 14580.
[138] P. Wang, K. Jiang, G. Wang, J. Yao, X. Huang, Angew. Chemie Int. Ed. 55 (2016) 12859–12863.
[139] H. Huang, K. Li, Z. Chen, L. Luo, Y. Gu, D. Zhang, C. Ma, R. Si, J. Yang, Z. Peng, J. Am. Chem. Soc. 139 (2017) 8152–8159.
[140] C. Koenigsmann, W.-p. Zhou, R.R. Adzic, E. Sutter, S.S. Wong, Nano Lett. 10 (2010) 2806–2811.
[141] K. Jiang, D. Zhao, S. Guo, X. Zhang, X. Zhu, J. Guo, G. Lu, X. Huang,Sci. Adv. 3 (2017), e1601705.
[142] L. Tao, D. Yu, J. Zhou, X. Lu, Y. Yang, F. Gao,Small 14 (2018), 1704503.
[143] S. Zhao, Y. Wang, J. Dong, C.-T. He, H. Yin, P. An, K. Zhao, X. Zhang, C. Gao, L. Zhang, Nat. Energy 1 (2016) 16184.
[144] J. Shen, Y. Zhu, H. Jiang, C. Li, Nano Today 11 (2016) 483–520.
[145] D. Voiry, J. Yang, M. Chhowalla, Adv. Mater. 28 (2016) 6197–6206.
[146] W. Yang, X. Zhang, Y. Xie, Nano Today 11 (2016) 793–816.
[147] M.A.Z.G. Sial, M.A.U. Din, X. Wang, Chem. Soc. Rev. 47 (2018) 6175–6200.
[148] H. Liu, P. Zhong, K. Liu, L. Han, H. Zheng, Y. Yin, C. Gao, Chem. Sci. 9 (2018) 398–404.
[149] X. Huang, S. Tang, X. Mu, Y. Dai, G. Chen, Z. Zhou, F. Ruan, Z. Yang, N. Zheng, Nat. Nanotech. 6 (2011) 28.
[150] Y. Pi, N. Zhang, S. Guo, J. Guo, X. Huang, Nano Lett. 16 (2016) 4424–4430.
[151] A.-X. Yin, W.-C. Liu, J. Ke, W. Zhu, J. Gu, Y.-W. Zhang, C.-H. Yan, J. Am. Chem. Soc. 134 (2012) 20479–20489.
[152] X. Kong, K. Xu, C. Zhang, J. Dai, S. Norooz Oliaee, L. Li, X. Zeng, C. Wu, Z. Peng, ACS Catal. 6 (2016) 1487–1492.
[153] H. Duan, N. Yan, R. Yu, C.-R. Chang, G. Zhou, H.-S. Hu, H. Rong, Z. Niu, J. Mao, H. Asakura, Nat. Commun. 5 (2014) 3093.
[154] Y. Kang, Q. Xue, P. Jin, J. Jiang, J. Zeng, Y. Chen, ACS Sustain. Chem. Eng. 5 (2017) 10156–10162.
[155] K. Wang, Y. Qin, F. Lv, M. Li, Q. Liu, F. Lin, J. Feng, C. Yang, P. Gao, S. Guo,Small Methods 2 (2018), 1700331.
[156] Y. Sun, Y. Liang, M. Luo, F. Lv, Y. Qin, L. Wang, C. Xu, E. Fu, S. Guo,Small 14 (2018), 1702259.
[157] H. Liao, J. Zhu, Y. Hou, Nanoscale 6 (2014) 1049–1055.
[158] Y. Zhang, M. Wang, E. Zhu, Y. Zheng, Y. Huang, X. Huang, Nano Lett. 15 (2015) 7519–7525.
[159] N. Yang, Z. Zhang, B. Chen, Y. Huang, J. Chen, Z. Lai, Y. Chen, M. Sindoro, A.L. Wang, H. Cheng,Adv. Mater. 29 (2017), 1700769.
[160] W. Chen, W. Gao, P. Tu, T. Robert, Y. Ma, H. Shan, X. Gu, W. Shang, P. Tao, C. Song, Nano Lett. 18 (2018) 5905–5912.
[161] L. Dai, Y. Zhao, Q. Qin, X. Zhao, C. Xu, N. Zheng, ChemNanoMat 2 (2016) 776–780.
[162] F. Saleem, Z. Zhang, B. Xu, X. Xu, P. He, X. Wang, J. Am. Chem. Soc. 135 (2013) 18304–18307.
[163] A. Mahmood, H. Lin, N. Xie, X. Wang, Chem. Mater. 29 (2017) 6329–6335.
[164] A. Mahmood, N. Xie, M.A.U. Din, F. Saleem, H. Lin, X. Wang, Chem. Sci. 8 (2017) 4292–4298.
[165] F. Lin, K. Wang, Y. Tang, J. Lai, M. Lou, M. Huang, S. Guo, Chem. Commun. (Camb.) 54 (2018) 1315–1318.
[166] Y. Qin, M. Luo, Y. Sun, C. Li, B. Huang, Y. Yang, Y. Li, L. Wang, S. Guo, ACS Catal. 8 (2018) 5581–5590.
[167] C. Tang, N. Zhang, Y. Ji, Q. Shao, Y. Li, X. Xiao, X. Huang, Nano Lett. 19 (2019) 1336–1342.
[168] Z. Fan, Y. Zhu, X. Huang, Y. Han, Q. Wang, Q. Liu, Y. Huang, C.L. Gan, H. Zhang, Angew. Chemie Int. Ed. 54 (2015) 5672–5676.
[169] W. Wang, Y. Zhao, Y. Ding, Nanoscale 7 (2015) 11934–11939.
[170] Y. Yan, H. Shan, G. Li, F. Xiao, Y. Jiang, Y. Yan, C. Jin, H. Zhang, J. Wu, D. Yang, Nano Lett. 16 (2016) 7999–8004.
[171] L. Bu, N. Zhang, S. Guo, X. Zhang, J. Li, J. Yao, T. Wu, G. Lu, J.-Y. Ma, D. Su, Science 354 (2016) 1410–1414.
[172] J. Fan, K. Qi, L. Zhang, H. Zhang, S. Yu, X. Cui, ACS Appl. Mater. Inter. 9 (2017) 18008–18014.
[173] J. Ding, Q. Shao, Y. Feng, X. Huang, Nano Energy 47 (2018) 1–7.

Yiju Li is currently a postdoctoral fellow under the supervision of Prof. Shaojun Guo at Peking University. He received his pH.D. degree in Materials Science and Engineering in 2018 from the Harbin Engineering University, China. His research interests include the design of advanced energy materials for electrochemical energy conversion and storage.

Shaojun Guo is a professor in the Department of Materials Science and Engineering, College of Engineering, Peking University, and a Fellow of the Royal Society of Chemistry. He is renowned for his leadership in nano/sub-nano/atomic materials for catalysis, energy and biomedical applications. Since his independence, he has published more than 100 papers as corresponding author in peer-reviewed journals like *Nature*, *Science* and *Nature Reviews Materials*, *etc* with 27,000-plus citations and an h-index of 88. He served as the associate editor of *ACS Omega*. Guo holds a BS in Materials Chemistry (2005) from Jilin University and a PhD in Analytical Chemistry (2010) from Changchun Institute of Applied Chemistry, Chinese Academy of Sciences.